(2)

HDL-TR-2172
February 1990

Experimental Demonstration of an Electromagnetically Pumped Free-Electron Laser with Cyclotron Harmonic Idlers

by R. Alan Kehs
Yuval Carmel
William W. Destler
Victor L. Granatstein

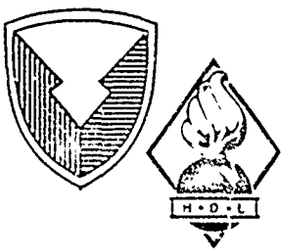

U.S. Army Laboratory Command
Harry Diamond Laboratories
Adelphi, MD 20783-1197

UNCLASSIFIED

SECURITY CLASSIFICATION OF THIS PAGE

REPORT DOCUMENTATION PAGE				Form Approved OMB No. 0704-0188
1a. REPORT SECURITY CLASSIFICATION Unclassified			1b. RESTRICTIVE MARKINGS	
2a. SECURITY CLASSIFICATION AUTHORITY			3. DISTRIBUTION/AVAILABILITY OF REPORT Approved for public release; distribution unlimited.	
2b. DECLASSIFICATION/DOWNGRADING SCHEDULE				
4. PERFORMING ORGANIZATION REPORT NUMBER(S) HDL-TR-2172			5. MONITORING ORGANIZATION REPORT NUMBER(S)	
6a. NAME OF PERFORMING ORGANIZATION Harry Diamond Laboratories	6b. OFFICE SYMBOL (If applicable) SLCHD-NW-RS		7a. NAME OF MONITORING ORGANIZATION	
6c. ADDRESS (City, State, and ZIP Code) 2800 Powder Mill Road Adelphi, MD 20783-1197			7b. ADDRESS (City, State, and ZIP Code)	
8a. NAME OF FUNDING/SPONSORING ORGANIZATION U.S. Army Laboratory Command	8b. OFFICE SYMBOL (If applicable) AMSLC		9. PROCUREMENT INSTRUMENT IDENTIFICATION NUMBER	
8c. ADDRESS (City, State, and ZIP Code) 2800 Powder Mill Road Adelphi, MD 20783-1145			10. SOURCE OF FUNDING NUMBERS PROGRAM ELEMENT NO.: 6.37.37 PROJECT NO.: TASK NO.: WORK UNIT ACCESSION NO.:	
11. TITLE (Include Security Classification) Experimental Demonstration of an Electromagnetically Pumped Free-Electron Laser with Cyclotron Harmonic Idlers				
12. PERSONAL AUTHOR(S) R. Alan Kehs (HDL), Yuval Carmel, William Destler, and Victor L. Granatstein (University of Maryland)				
13a. TYPE OF REPORT Summary	13b. TIME COVERED FROM Jan 87 TO June 88		14. DATE OF REPORT (Year, Month, Day) February 1990	15. PAGE COUNT 75
16. SUPPLEMENTARY NOTATION AMS code: 623737.000; HDL Project No. FE7927				
17. COSATI CODES FIELD / GROUP / SUB GROUP			18. SUBJECT TERMS (Continue on reverse if necessary and identify by block number) Free electron laser, high power microwave	

19. ABSTRACT (Continue on reverse if necessary and identify by block number)

A new type of electromagnetically pumped, three-wave free-electron laser (FEL) has been observed in which cyclotron harmonic waves act as idlers. In this experiment, a powerful electromagnetic "pump" wave replaced the usual magnetostatic wiggler. The pump wave was generated by a backward wave oscillator (8.4 GHz, 50 MW peak power) driven by an intense relativistic electron beam (625 kV, 2 kA, 100 ns). A grating spectrometer was used to scan the microwave frequency spectrum from 50 to 130 GHz, and powerful high-frequency radiation was observed in the form of an array of regularly spaced peaks. The positions of the peaks were observed to vary with the magnitude of the axial guide magnetic field in a manner which agrees with the dispersion relationship

$$\omega_s = \omega_w + k_w v_z + k_s v_z + l\Omega_0$$

(cont'd)

20. DISTRIBUTION/AVAILABILITY OF ABSTRACT	21. ABSTRACT SECURITY CLASSIFICATION	
☒ UNCLASSIFIED/UNLIMITED ☐ SAME AS RPT ☐ DTIC USERS	Unclassified	
22a. NAME OF RESPONSIBLE INDIVIDUAL R. Alan Kehs	22b. TELEPHONE (Include Area Code) (202) 394-4143	22c. OFFICE SYMBOL SLCHD-NW-RS

DD Form 1473, JUN 86 — Previous editions are obsolete — SECURITY CLASSIFICATION OF THIS PAGE

UNCLASSIFIED

19. Abstract (cont'd)

due to a three-wave FEL interaction in which the cyclotron beam waves act as "idlers" where (ω_s, k_s) and (ω_p, k_p) are the frequency and wave number of scattered and pump waves, Ω_e is the relativistic electron cyclotron frequency, l is the harmonic number, and v_z is the axial beam velocity. We identified harmonic numbers $l = 1$ and 5 to 14 while sweeping through the frequency ranges from 7 to 18 GHz and 50 to 150 GHz. The results exhibit excellent agreement with a simple theoretical model of the three-wave interaction.

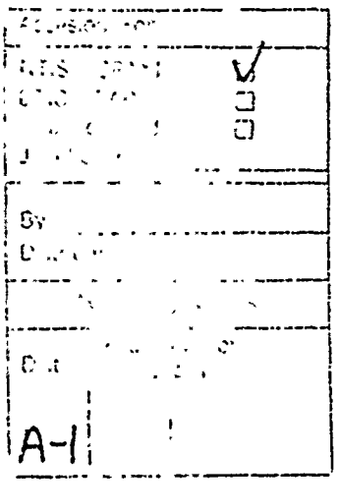

Contents

Contents (cont'd)

Figures

Figures (cont'd)

Tables

1. Introduction

In previous experiments Carmel [1] and Denisov [2] have recorded high-frequency microwave radiation that was attributed to a two-stage backward-wave oscillator/free-electron laser (FEL), but this report represents the first careful study of the detailed frequency spectrum produced by such a device. In these experiments, a backward wave oscillator driven by a high-power relativistic electron beam was used to produce a high-intensity pulse of microwave radiation that propagates antiparallel to the electron beam. The ensuing microwave spectrum was then scanned from 50 to 130 GHz, with the unexpected result that the spectrum was composed of an array of regularly spaced peaks whose positions varied with changes in the applied magnetic guide field. The measured data show excellent agreement with a three-wave FEL interaction model utilizing a backward propagating pump wave and cyclotron harmonic idler waves. Although this is primarily an experimental report, a brief derivation and discussion of the interaction model will be presented.

First, some perspective is provided by a brief review of the classical FEL (magnetostatic wiggler) and its historical development. This is followed by a short description of the electromagnetically pumped FEL. Later sections provide an "in depth" look at the experimental setup, the basic theory that was used to describe the interaction, and a complete discussion of the results.

The most basic model of a FEL is a two-wave interaction in which a transverse, periodic, magnetic field induces oscillations on an intense, energetic electron beam. In the configuration shown in figure 1, an electron beam is injected along the $\hat{z}$-axis so that it will pass through the spatially varying magnetic field generated by the permanent bar magnets labeled N and S. At the point of interaction, the electrons have random phase and radiate incoherently. However, a ponderomotive force is produced by the action of the induced $v_\perp$ (often called the quiver velocity) and the radiation or scattered wave. That is, from the Lorentz force law,

$$F_{pond} = -|e| v_\perp \times B_s, \tag{1}$$

where e is the electronic charge, $v_\perp$ is the quiver velocity, and B_s is the magnetic component of the electromagnetic wave. This $\hat{z}$-directed

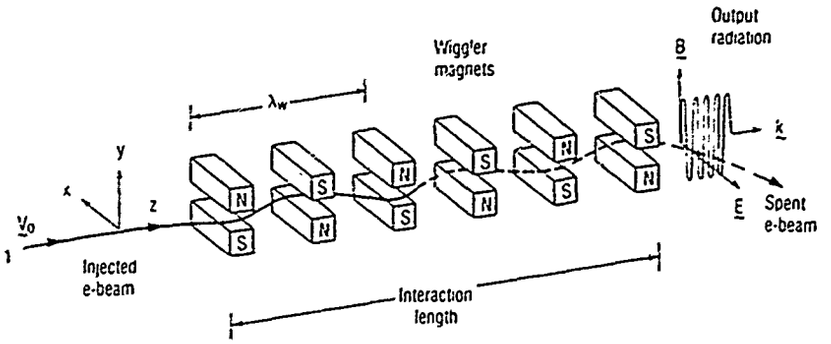

Figure 1. Basic magnetostatically pumped free electron laser (FEL) interaction.

force acts to push the electrons into axial bunches. The ponderomotive force causes some electrons to be accelerated and others to be decelerated. If the axial velocity v_{z0} is such that more electrons are decelerated, then the average energy of the electrons decreases and the radiation field is enhanced. Clearly, this process will proceed only when the oscillating electrons are properly synchronized with the electromagnetic wave. The synchronism condition also leads to a relation for the frequency spectrum of the ideal magnetostatic model given by

$$\omega = \beta(1+\beta)\gamma^2 c k_w, \tag{2}$$

where β is the normalized axial beam velocity, c is the speed of light, and $k_w = 2\pi/\lambda_w$, where λ_w is the magnetic wiggler period. This is equivalent to

$$\lambda = \lambda_w/2\gamma^2. \tag{3}$$

The above analysis is appropriate for a low-density electron beam in which single particle equations can be used to describe the interaction—this is called the Compton regime. For higher density electron beams, collective effects become important and beam waves or "idlers" can participate in a three-wave interaction—this is called the Raman regime. FEL devices are also categorized by the type and strength of the "wiggler." Although a magnetostatic wiggler was used in the above example, any field that leads to a transverse velocity modulation of the electron beam can be used as a wiggler. Several other types of wigglers have been proposed—including electrostatic [3], magnetic quadrupole [4-5], and of course the electromagnetic pump wave, which will be discussed more thoroughly in this report.

This classical FEL was first described by Motz in 1951, when he proposed a method for generating high-frequency radiation via the synchrotron radiation from electron oscillations in a periodic magnetic field [6]. Although Motz conducted several experiments to test his theory [7], the first practical devices to exploit this approach were developed in the late 1950's and early 1960's by R. M. Philips, who called his device the "ubitron" [8-10]. While propagating a 110- to 140-kV electron beam through a linear wiggler, Phillips was able to generate 1 MW of power at 10-percent efficiency by operating the device as an amplifier (gain $\sim$ 13 dB). Because of strong competition from gyrotrons, ubitron research was halted in 1964, but has recently been restarted [11].

Theoretical analyses of FEL configurations began to appear in the late 1960's and early 1970's [12-16]. These papers featured quantum mechanical models to predict that FEL-type devices could be operated as both oscillators and amplifiers at infrared and millimeter wavelengths; that is, they could "fill the gap" by providing high-power sources in the region between conventional lasers and conventional microwave tubes. Interest in these calculations led researchers at Stanford University to the operation of both a Compton FEL amplifier [17] in 1976 and an oscillator [18] in 1977.

Although Compton FEL experiments have been successful in generating respectable power levels at very high frequencies, they are inherently low-gain devices which require long (many wiggler period) interaction regions and large sophisticated particle accelerators to produce the high γ beams. As a result, researchers began to study millimeter-wave FEL's which operated in the Raman regime, where higher gain and efficiency can be achieved. The first experiments in the Raman regime used high-power cyclotron maser radiation as the pump field for the FEL interaction [19]. Initially, a 2-MV, 30-kA electron beam was used to generate 1 MW of power in the 400- to 500-μm range [20]. Later a magnetostatic undulator was used on a 1.2-MV, 25-kA electron beam to produce $\sim$1 MW of power at 400 μm [21]. Further experiments at the Naval Research Lab (NRL) generated as much as 100 MW of power at frequencies ranging from 50 to 100 GHz [22,23]. Recently, more sophisticated experimental setups [24,25] with better quality electron beams have begun to show excellent agreement with the more sophisticated three-dimensional [26] and nonlinear [27,28] theories that have been developed.

Although difficulties in generating a sufficiently strong pump wave have kept the electromagnetically pumped FEL in the background, the scheme remains attractive because of the larger frequency shift factor

associated with electromagnetically pumped rather than magnetostatically pumped FEL's. That is, for an electromagnetically pumped FEL,

$$\omega = 4\gamma^2\omega_w, \tag{4}$$

in the high γ limit where space charge effects have been ignored and ω_w is the pump frequency. Note that this frequency shift is twice as large as the factor for the magnetostatically pumped case given in equation (3).

Interest in electromagnetically pumped FEL's has recently been rekindled by the development of high-power backward wave oscillators (BWO's) [1,29-31]. These devices produce an intense electromagnetic wave that propagates counter to the electron beam and acts as an electromagnetic pump on the electron beam. In experiments at NRL [1], a 500-MW, 12.5-GHz pump wave was used to produce radiation at frequencies greater than 140 GHz via an FEL interaction. Similar experiments by Denisov et al. using a 500-MW, 10-GHz pump and a 600- to 650-keV, 3- to 5-kA electron beam have produced as high as 10 MW at frequencies between 50 and 100 GHz [2,32]. This report focuses on a detailed examination of the high-power-microwave frequency spectrum produced by an electromagnetically pumped FEL.

From the schematic representation shown in figure 2, we see an electron beam guided through a slow-wave structure by an applied B_z. The BWO pump wave grows and interacts with the electron beam until it reaches the slow-wave structure's beam entrance section which has a cutoff frequency beyond that of the 8.4-GHz pump wave. The pump wave is then reflected and propagates back with the electron beam through the slow-wave structure. As the electron beam exits the slow-wave structure, the divergence of the axial field causes the beam to "dump" on the side walls while the reflected pump wave continues to propagate to the right, where it passes through a region of high power microwave diagnostics that are not shown on the figure. In addition to guiding the electron beam, the applied magnetic field also enables the growth of cyclotron waves on the beam, which will play an important role in the analysis of the data.

Theoretical models and descriptions of the experiment are introduced in section 2. Section 3 provides a detailed overview of the experimental setup that was used to record the data used in this report. This is followed by a presentation and discussion of the experimental results. The final section summarizes key points, conclusions, and recommendations for future work.

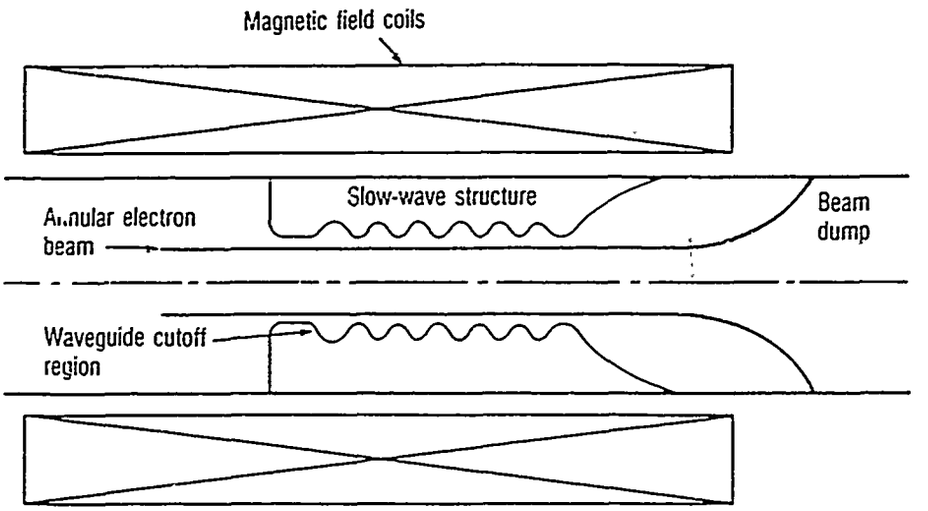

Figure 2. Basic electromagnetically pumped FEL configuration.

2. Theory

2.1 Calculation of Expected Frequency Shifts

Although a presentation of the full theory of the electromagnetically pumped FEL is beyond the scope of this report, the portions of theory needed to predict the simple output spectrum are presented in detail. First, some perspective is provided by a brief review of the "classical" magnetostatic FEL. This is followed by a description of the electromagnetically pumped FEL and, finally, a discussion of some related processes such as the cyclotron harmonic autoresonant maser (CHARM).

The most basic model of a FEL is a two-wave interaction in which a transverse, periodic, magnetic field induces oscillations on an intense, energetic electron beam. Again, using the configuration shown in figure 1, an electron beam is injected along the $\hat{z}$-axis so that it will pass through the spatially varying magnetic field generated by the permanent bar magnets labeled N and S. At the point of interaction, the electrons have random phase and radiate incoherently. However, a ponderomotive force is produced by the action of the induced $v_\perp$ (often called the quiver velocity or wiggler velocity) and the radiation or scattered wave. That is, from the Lorentz force law,

$$F_{pond} = -|e|v_\perp \times B_s, \tag{4}$$

where $|e|$ is the electronic charge, $v_\perp$ is the wiggler velocity, and B_s is the magnetic component of the scattered electromagnetic wave. This $\hat{z}$-directed force acts to push the electrons into axial bunches. The ponderomotive force causes some electrons to be accelerated and others to be decelerated. If the axial velocity of the beam v_{z0} is such that more electrons are decelerated, then the average energy of the electrons decreases and the radiation field is enhanced. Clearly, this process will proceed only when the oscillating electrons are properly synchronized with the electromagnetic wave. This synchronism condition leads directly to a relation for the expected frequency spectrum of the ideal magnetostatic FEL model.

One may evaluate this simple model by approximating the magnetostatic "pump" field as

$$B_y = B_w \cos(k_w z), \tag{5}$$

where $k_w = 2\pi/L$, L is the magnet period, and B_w is the magnitude of the "pump" field. The equation of motion is given by

$$\gamma m \dot{v}_x = \frac{e}{c}[v_y \times B_z - v_z \times B_y], v_z \gg v_y, \tag{6}$$

where γ is the relativistic factor, m is the mass of an electron, and c is the speed of light. With $B_z = 0$, this has solution

$$\dot{v}_x = -\frac{eB_w}{\gamma mc} \cos(k_w z) v_{z0} \rightarrow -\Omega_w v_{z0} \cos(k_w z), \tag{7}$$

which may be integrated by assuming that $\omega_w = k_w v_{z0}$ and $z = v_{z0} t$. This yields a form for the wiggler velocity given by

$$v_x = \frac{\Omega_w v_{z0}}{\omega_w} \sin(\omega_w t). \tag{8}$$

The radiation field may be expressed as

$$\mathrm{B}_s = B_s [\sin(k_s z - \omega_s t)], \tag{9}$$

where (ω_s, k_s) represents the frequency and wavenumber of the scattered wave. The ponderomotive force then becomes

$$\mathrm{F}_{pond} = \frac{e}{c} \frac{\Omega_w v_{z0}}{\omega_w B_s} \sin(k_w z) \sin(k_s z - \omega_s t). \tag{10}$$

The sine factors that comprise the phase portion of the ponderomotive force can now be combined via trigonometric identities to yield a term

proportional to $\cos(k_w z + k_s z - \omega_s t)$. Clearly, the ponderomotive force will reach a maximum when the phase $(\psi = k_w z + k_s z - \omega_s t) \rightarrow 0$. The phase velocity of the ponderomotive wave can then be written as

$$v_{ph} = \frac{\omega_s}{k_w + k_s}. \tag{11}$$

Synchronism between the electron beam and the ponderomotive force can be achieved when $v_{ph} \approx v_{z0}$, the velocity of the electron beam. For a relatively high-frequency wave (wavelength is small compared to external boundaries), one may write $\omega_s = k_s c$, where c is the speed of light. This may be combined with equation (11) to give

$$k_w \beta = k_s(1 - \beta), \tag{12}$$

where $\beta \equiv v_{z0}/c$. Noting that γ, the relativistic factor, may be expressed as $\gamma^{-2} = (1 + \beta)(1 - \beta)$, and recalling that $\lambda = 2\pi/k$, one may rewrite equation (12) as

$$\lambda_s = \frac{\lambda_w}{\gamma^2 \beta(1 + \beta)}. \tag{13}$$

For $\beta \rightarrow 1$, this reduces to the familiar form

$$\lambda_s = \frac{\lambda_w}{2\gamma^2}. \tag{14}$$

For an electromagnetic pump, $B_y \rightarrow B_0 \sin(k_0 z - \omega_0 t)$, which results in a ponderomotive force phase of

$$\psi_{em} = k_w z + k_s z + \omega_w t - \omega_s t. \tag{15}$$

The resulting phase velocity is then

$$v_{ph} = \frac{\omega_s - \omega_w}{k_w + k_s} \rightarrow v_{z0}. \tag{16}$$

Again assuming that $\omega_s = k_s c$ and now writing that $\omega_w \equiv k_w v_{ph}$, one can combine to form [33]

$$\omega_s = \gamma^2(1 + \beta)(1 + v_{z0}/v_{ph})\omega_w. \tag{17}$$

With the usual but not always justifiable assumptions that $\beta \rightarrow 1$ and $v_{ph} \rightarrow c$, this expression can be further reduced to the familiar

$$\omega_s \cong 4\gamma^2 \omega_w. \tag{18}$$

A more rigorous derivation of the quiver velocity or wiggler velocity produced by an electromagnetic pump wave can be found elsewhere [34, 35]. As expected, the more rigorous derivation produces an identical relation for the frequency of the scattered radiation.

These same results may also be reached by modeling the process as Compton scattering in the rest frame of the electron beam. The sinusoidally varying magnetostatic pump field of figure 3 will appear as a Doppler-shifted propagating electromagnetic wave in the electron beam's rest frame. This wave will scatter off the electron beam and be frequency-shifted a second time by the transformation back to the laboratory frame of reference.

In the laboratory frame, incoming pump and scattered waves are represented by (ω_w, k_w) and (ω_s, k_s). In the rest frame of the electron beam,

$$(\omega_w, k_w) \rightarrow (\omega'_w, k'_w)$$

and

$$(\omega_s, k_s) \rightarrow (\omega'_s, k'_s). \tag{19}$$

The overall wave traffic is shown in figure 3. One may now construct the invariant 4-vector as in Jackson [36],

$$\frac{\tilde{\omega}}{c} = (\frac{\omega}{c}, \mathrm{k}). \tag{20}$$

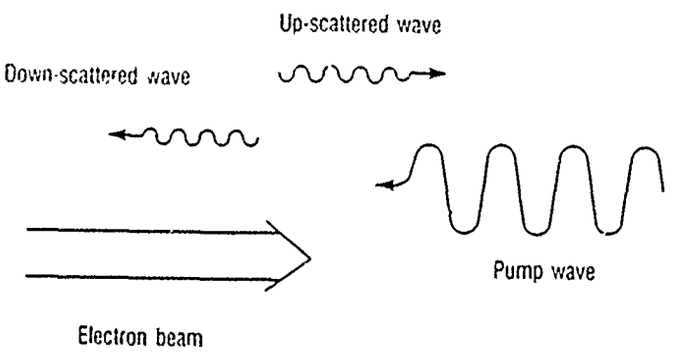

Figure 3. Wave direction conventions in two-wave electromagnetically pumped FEL interaction model.

Then with K as the lab frame and K' as the beam frame, one can look at the waves in the rest frame of the electron beam. That is,

$$\frac{\omega'_w}{c} = \gamma(\frac{\omega_w}{c} + \frac{v_{z0}}{c}k_w),$$
$$\frac{\omega'_s}{c} = \gamma(\frac{\omega_s}{c} + \frac{v_{z0}}{c}k_s), \tag{21}$$

where v_{z0} is the velocity of the electron beam. Now use the Manley-Rowe equations to write

$$\gamma(\omega_w + v_{z0}\frac{\omega_w}{v_{ph}}) = \gamma(\omega_s - \frac{v_{z0}}{c}\omega_s)$$

or

$$\omega_s = \gamma^2(1+\beta)(1+v_{z0}/v_{ph})\omega_w. \tag{22}$$

For the static magnetic wiggler case, $\omega_w \to 0$ and one uses $\omega_s = k_s c$ to eliminate ω_s and form

$$\gamma(v_z k_w) = \gamma(k_s c - k_s v_z),$$

which can be combined to form the familiar

$$\lambda_s = \frac{\lambda_w}{\gamma^2\beta(1+\beta)}. \tag{23}$$

Since these experiments are generally carried out inside some sort of waveguide, the electromagnetic mode $\omega_s = k_s c$ should be replaced with

$$\omega_s^2 = k_s^2 c^2 + \omega_c^2, \tag{24}$$

where ω_c is the effective cutoff frequency of the waveguide. This correction will be used in later sections and in all computations.

It is also constructive to consider a graphical representation of the FEL interaction. From equation (16) with $v_{ph} = v_{z0}$, the resonance condition yields

$$\omega_s - \omega_w = (k_s + k_w)v_{z0}. \tag{25}$$

This resonance condition may then be plotted with the electromagnetic waveguide mode represented by equation (24) to obtain the dispersion relation shown in figure 4. The two points (ω, k) where the electron beam and the scattered wave are in phase represent points where energy can be transferred from the beam to the wave.

This analysis is appropriate for low-density electron beams in which single particle equations can be used to describe the interactions—the Compton operating regime of the FEL. For higher density electron beams, collective effects become important and beam waves or idlers can participate in a more complicated three-wave interaction—the Raman regime. The FEL described in this report operates in this high-beam-density Raman regime.

The basic approaches used to describe the expected output from a two-wave FEL interaction can be expanded to include the effect of the third "idler" wave that participates in the three-wave interaction described in this report.

A high-current electron beam propagating through an axial magnetic field can support several types of "beam idlers" [37]. The most important types (and the only ones that will be considered in this report) are the negative-energy space-charge and cyclotron waves. They are called negative energy because they grow in amplitude as energy is lost from the electron beam. They are important because they can act with the pump wave to efficiently couple energy from the electron beam into "scattered radiation" via a three-wave interaction.

In the following approach adapted from Marshall [38], the three-wave FEL is studied in the rest frame of the electron beam by considering the interaction of the pump wave (ω'_w, k'_w), the scattered wave

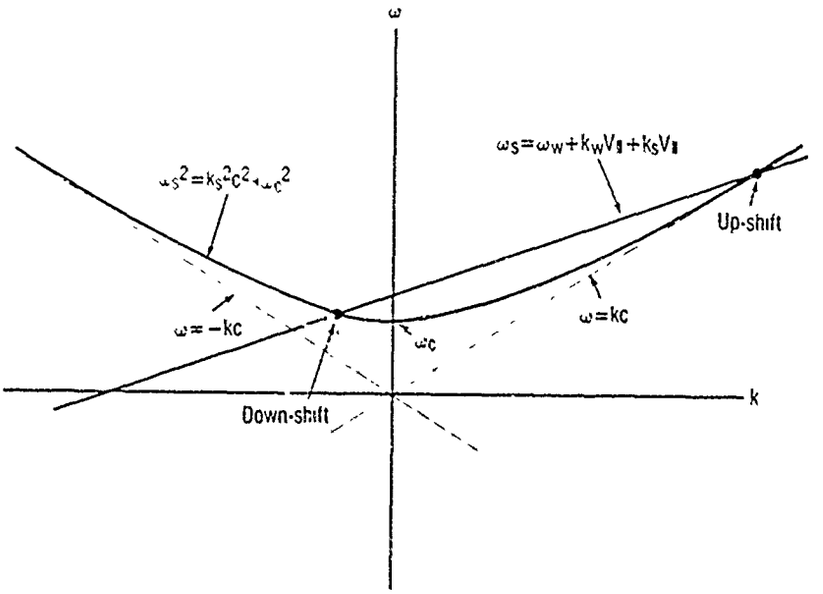

Figure 4. Dispersion diagram for two-wave FEL interaction.

(ω_s', k_s'), and the beat or idler wave (ω_i', k_i'). The idler arises from the ponderomotive bunching of the electrons via the force term given by

$$\frac{e}{c}[\mathbf{v}_w'(\omega_w') \times \mathbf{B}_s'(\omega_s')], \tag{26}$$

where the primes indicate the shift to the electon-beam rest frame. The interaction occurs at $\omega_w' - \omega_s'$, leading to

$$\omega_i' = \omega_w' - \omega_s'$$

and

$$k_i' = k_w' + k_s' \tag{27}$$

for the idler frequency and wavenumber. The idler or "beat" wave is always present, but the interaction is enhanced whenever ω_i' corresponds to a "natural" resonant frequency of the system; i.e., $\omega_i' = \omega_p'$, or $\omega_i' = \Omega_0'$, where ω_p' and Ω_0' represent the beam plasma frequency and electron cyclotron frequency in the rest frame of the electron beam. The three-wave interaction $\omega_p' = \omega_w' - \omega_s'$ is referred to as "stimulated Raman scattering." This effect is shown graphically in figure 5. The parallelogram relating the three waves follows from equation (28):

$$\omega_i' = \omega_w' - \omega_s'$$

and

$$k_i' = k_w' + k_s'. \tag{28}$$

It should be remembered that this model is somewhat oversimplified, involving uncoupled modes of the system. The actual situation is far more complicated when mode coupling occurs.

One can also study the effect of idlers by their influence on the beam resonance condition. Based on equation (28), there will be an additional shift in the frequency, so that the resonance condition becomes

$$\omega_s - \omega_w = k_w v_\parallel + k_s v_\parallel - \omega_{idler}. \tag{29}$$

The derivation of similar relations is described in more detail in the references [39].

For the space charge idler, the relation becomes

$$\omega_s - \omega_w = k_w v_\parallel + k_s v_\parallel \mp \omega_b, \tag{30}$$

where ω_b is the plasma frequency of the electron beam and the $+/-$ signs represent the positive/negative-energy space charge waves which are also discussed in detail by Johnson [39]. This effect has recently

been the subject of careful study in a series of Raman regime experiments at the Massachusetts Institute of Technology [25,40].

A typical dispersion relation for a Raman-regime FEL with space charge idlers is shown in figure 6. The wave of interest is the slow or negative-energy space charge wave because it is able to grow by "feeding" from the electron beam's kinetic energy. Note that two intersections or operating points are possible which yield both an up-shifted and a down-shifted frequency. Although (in a classic FEL) one is generally interested in the up-shifted frequency, the down-shifted frequency is also present [25,40].

Although frequency shifts in Raman FEL experiments have been traced to cyclotron wave idlers [41-43], the observation of cyclotron wave harmonics as idlers is new [44]. Their effect is similar to the space charge waves with a resonance condition now given by

$$\omega_s - \omega_w = k_w v_\parallel + k_s v_\parallel + \ell\Omega_0, \tag{31}$$

where Ω_0 is the effective relativistic electron cyclotron frequency and ℓ is the integer harmonic number.

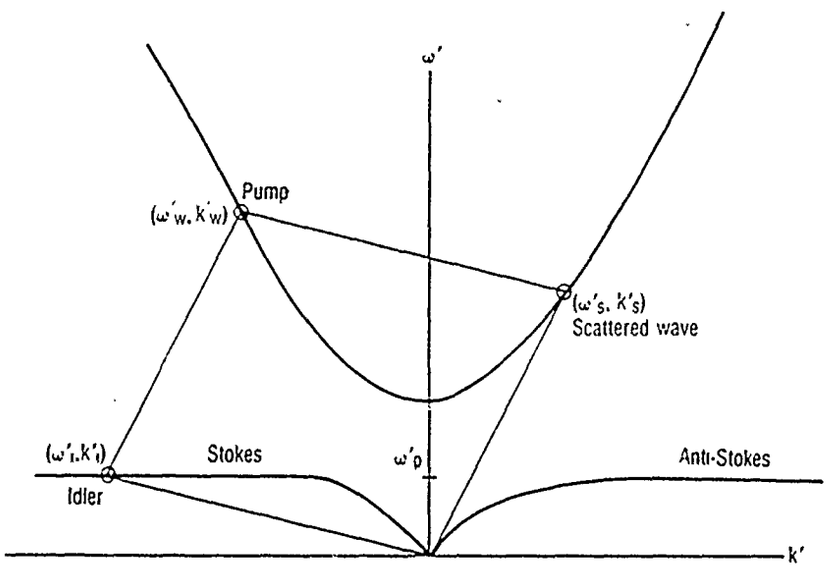

Figure 5. Stokes diagram of three-wave scattering relationship in electron rest frame with a space charge idler.

The idealized dispersion relation for the electromagnetically pumped FEL with cyclotron harmonic idlers is shown in figure 7. There are two allowed interaction frequencies for each harmonic number: an "up-shifted" frequency and a "down-shifted" frequency. Actually, both interaction frequencies are generally higher than the pump frequency, but convention refers to the higher as up-shifted and the lower as down-shifted. In figure 7, the up-shifted interaction frequencies are marked with squares while the lower down-shifted interaction frequencies are marked with circles. In either case, the interaction would be expected to produce a spectrum of regularly spaced peaks. In the next section, these predicted frequency spectra are examined in more detail, with emphasis on their dependence on the applied axial magnetic field.

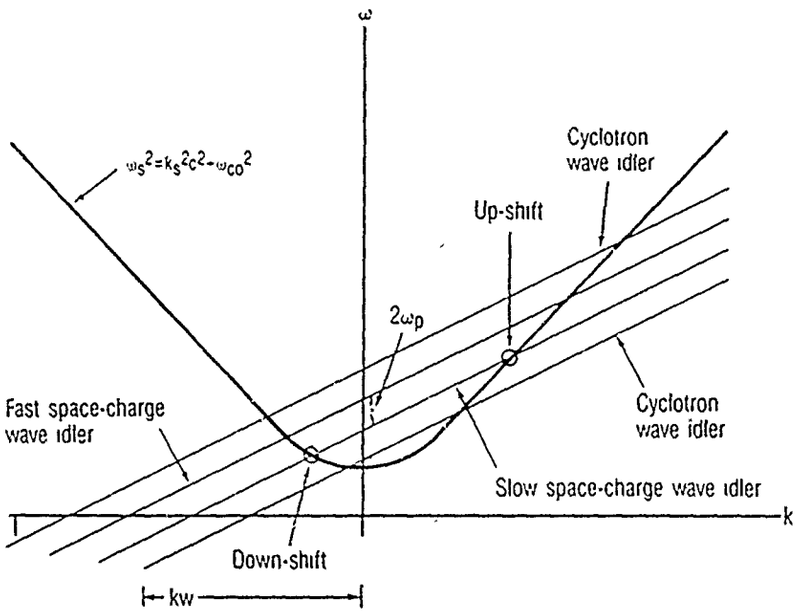

Figure 6. Idealized dispersion diagram for electromagnetically (EM) pumped FEL with space charge idler.

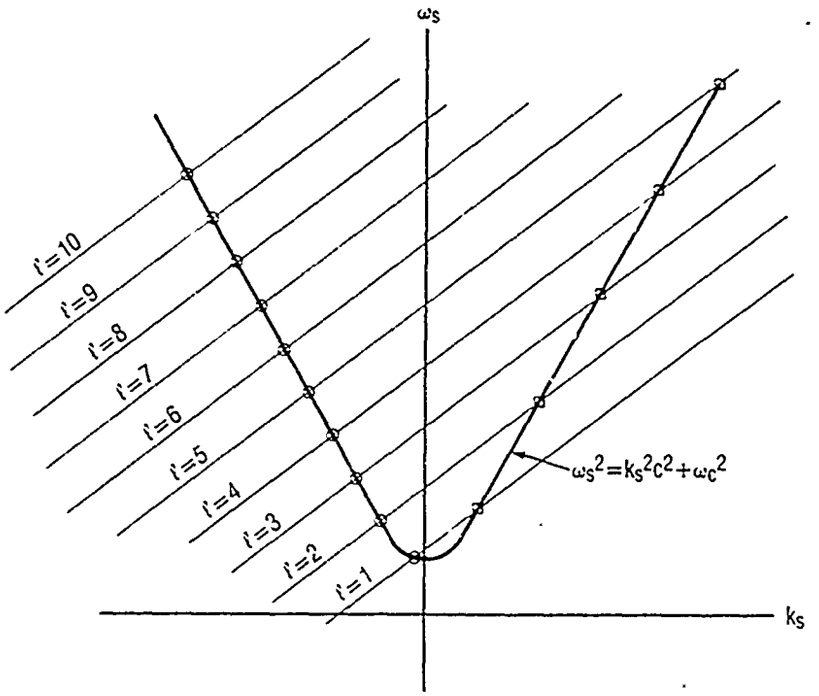

Figure 7. Idealized dispersion diagram for EM pumped FEL with cyclotron harmonic idlers.

2.2 Frequency Spectra

In order to facilitate the calculation of the frequency spectra in different physical situations, a result will be derived in terms of an effective k_w that will be designated k_{eff}. Plots of the spectra from appropriate physical situations will be used to analyze the experimental results in a later section. In the equations that follow, $\beta_{\|} = v_{z0}/c$ and $\gamma_{\|}^{-2} = 1 - \beta_{\|}^2$ will be used to emphasize the difference between $\beta_{\|}$ and β_{ph}.

2.2.1 Magnetostatic Wiggler

For the case of the magnetostatic wiggler, it is appropriate to use equation (25) with $\omega_w = 0$ and $k_w = k_{eff}$. This can be combined with equation (24) to yield

$$\omega_s = \beta_{\|} c k_{eff} \gamma_{\|}^2 \left[1 \pm \beta_{\|} \sqrt{1 - \left(\frac{\omega_c}{\beta_{\|} \gamma_{\|} c k_{eff}} \right)^2} \right], \qquad (32)$$

which is the normal result for a magnetostatic pump wave. Note that the +/− signs represent the up/down-shifted branches of the interaction, that is, the square/circle points in figure 6.

2.2.2 *Electromagnetic Wiggler*

In order to cast the electromagnetic wiggler in terms of k_{eff}, it is useful to define $\beta_{ph} \equiv -\omega_w/k_w c$, where the minus sign indicates that the pump is a backward propagating wave. This can be used in conjunction with equation (25) to produce

$$k_{eff} = \frac{\omega_w}{\beta_{\|} c}\left[1 + \frac{\beta_{\|}}{\beta_{ph}}\right], \tag{33}$$

which may be used in equation (32) to produce a spectrum given by

$$\omega_s = \omega_w \gamma_{\|}^2 (1 + \beta_{\|}/\beta_{ph})\left[1 \pm \beta_{\|}\sqrt{1 - \left(\frac{\omega_c}{\beta_{\|}\gamma_{\|} c k_{eff}}\right)^2}\right]. \tag{34}$$

Note that when the waveguide effects are ignored ($\omega_c = 0$), equation (34) reduces to the familiar result given by equation (22). These formulas must now be further "corrected" to include the effects of the beam idlers.

For space charge waves, the effective k_w is given by

$$k_{eff} = \frac{\omega_w}{\beta_{\|} c}\left[1 + \frac{\beta_{\|}}{\beta_{ph}}\right] \pm \frac{\omega_p}{\beta_{\|} c}, \tag{35}$$

where the +/− signs represent the fast/slow, positive/negative-energy space charge waves. In actual practice, only the slow, negative-energy wave can help to couple the beam's kinetic energy into electromagnetic radiation.

For cyclotron harmonic idlers, the effective k_w is given by

$$k_{eff} = \frac{\omega_w}{\beta_{\|} c}\left[1 + \frac{\beta_{\|}}{\beta_{ph}}\right] + \frac{\ell\Omega_0}{\beta_{\|} c}, \tag{36}$$

which results in a frequency spectrum represented by

$$\omega_s = \gamma_{\|}^2\left[\omega_w\left(1 + \frac{\beta_{\|}}{\beta_{ph}}\right) + \ell\Omega_0\right]\left[1 \pm \beta_{\|}(wge)\right]. \tag{37}$$

Although they were included in the calculations, the waveguide effects (*wgc*) are generally unnoticeable at high frequencies ($\ell > 4$); however, they modify the final $\beta_{\|}$ term by

$$\beta_{\|} \rightarrow \beta_{\|}\left[1 - \left(\frac{\omega_c/\gamma_{\|}}{\omega_w(1+\beta_{\|}/\beta_{ph}) + \ell\Omega_0}\right)^2\right]^{1/2}. \qquad (38)$$

It is important to note that equation (37) gives the expected frequency spectra versus applied magnetic field for four situations of interest: a "backward" propagating pump wave, up or down shifted, and "forward" propagating pump wave, up or down shifted. The forward pump situation must be considered because (as we see in the next section) in the actual experiment, the BWO pump wave reflects off a section of waveguide beyond cutoff (near the diode) and travels back through the slow-wave structure before finally exiting the system.

A graphical representation of equation (37) is provided in figure 8. If a value is chosen for the applied magnetic field, a whole spectrum of regularly spaced peaks should be produced by the interaction. Although some of the even harmonics were omitted from the plot in order to reduce overcrowding, all harmonics should be present in any spectrum which can be modeled by equation (37).

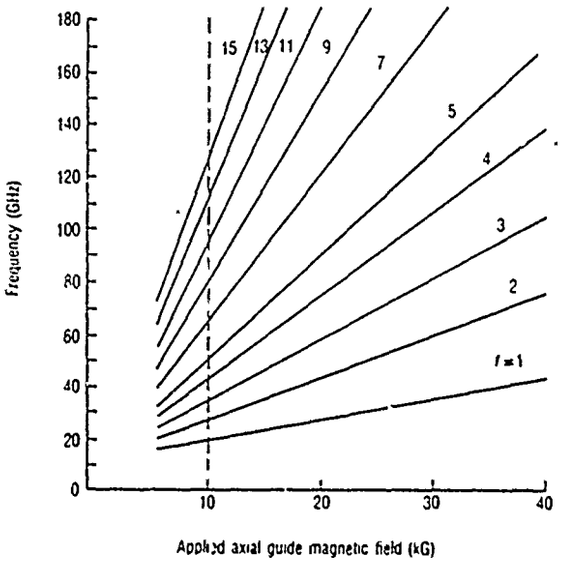

Figure 8. Plot of interaction frequency versus applied magnetic field for several harmonics of EM-pumped FEL with cyclotron harmonic idlers.

2.3 The CHARM Interaction

In the previous section, cyclotron harmonic waves were considered idlers in a three-wave FEL interaction. The possibility also exists that the observed spectrum of regularly spaced high-frequency peaks may be due directly to the cyclotron waves—with no FEL type of interaction.

The cyclotron autoresonant maser (CARM) is a well known producer of high-power microwave radiation [45, 46]. The term "CHARM" was coined to describe harmonic radiation from the basic CARM process. Although the history and detailed theory of the CHARM lie beyond the scope of this report, it is necessary to consider the frequency spectrum of such a device in order to help prove that the proper model has been chosen to explain the experimental data.

The simplest approach is to begin with equation (37) in the previous section. If the FEL term is deleted and the "idler" term is retained, the effective k_w is given by

$$k_{eff} = \frac{\ell\Omega_0}{\beta_{\|}c}, \tag{39}$$

which yields a properly Doppler-shifted frequency spectrum of

$$\omega_s = \gamma_{\|}^2 \ell\Omega_0 \left[1 \pm \beta_{\|}\sqrt{1 - \left(\frac{\omega_c/\gamma_{\|}}{\ell\Omega_0}\right)^2}\right]. \tag{40}$$

Clearly this relation leads to the same spacing between peaks, and at high frequencies where $\ell\Omega_0 \gg \omega_w[1 + \beta_{\|}/\beta_{ph}]$, the FEL and CHARM spectra will be virtually identical—except for a relatively small frequency shift. However, at low frequencies ($\ell = 1$ or 2), the frequency difference is significant and the differences are readily apparent. In a later section, these differences are more fully explored when the actual experimental data are presented.

3. Experimental Configuration

This section provides an overview of the basic experimental setup, followed by a detailed look at the major individual components and the diagnostics used to measure and record the data.

3.1 Introduction and Outline

The basic experimental configuration is shown in figure 9. An intense relativistic electron beam (650 kV, 2 kA, 100 ns) is produced by driving

an annular, field-emission cathode with the Dragon pulse generator. The axial magnetic field then guides the beam through the foilless anode and slow-wave structure to the beam dump region. The rippled-wall slow-wave structure allows the beam to couple kinetic energy into the structure's TM_{01} backward propagating mode at 8.4 GHz, providing the pump wave for the FEL interaction.

In the principal mode of operation illustrated in figure 10, the backward pump wave grows in strength and drives the FEL interaction as it propagates towards the "cutoff" region. The scattered radiation follows the same path, except that its reflection from the cutoff region is not as complete as for the lower frequency pump wave. Thus it is the reflected waves that finally reach the microwave diagnostics region. In a later section, it is also shown that the reflected waves do not interact with the electron beam.

3.2 The Intense Relativistic Electron Beam

The intense relativistic electron beam used in these experiments is produced by an annular field-emission cathode driven by the Dragon pulse generator [47]. In the Dragon machine, a capacitive energy store is resonantly discharged through a voltage step-up transformer to a coaxial, water dielectric, transmission line. When the voltage on the transmission line reaches its peak, a self-breaking switch feeds the stored energy to the diode. A more detailed description of the Dragon pulser is given in appendix A.

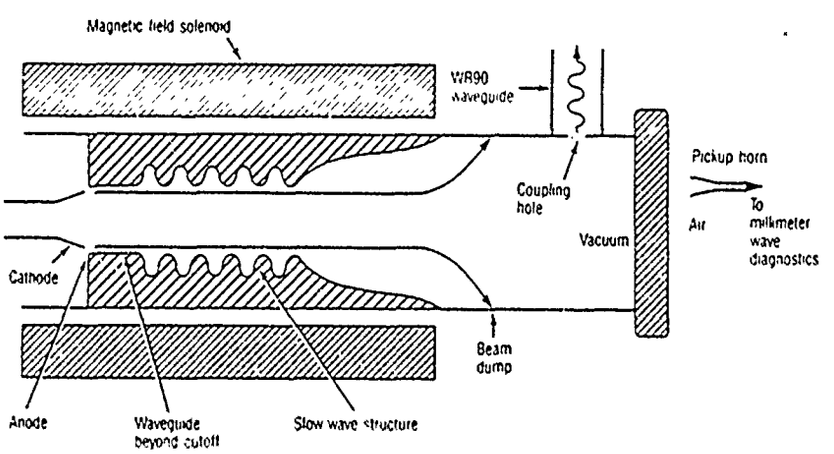

Figure 9. Basic experimental configuration used for EM-pumped FEL experiments.

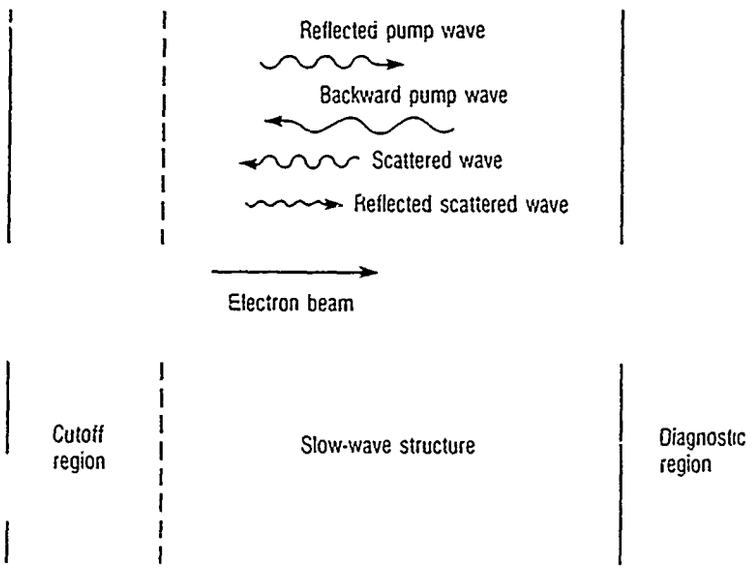

Figure 10. Principal wave traffic in the EM-pumped FEL experiment.

The Dragon pulser is tuned to deliver a relatively flat 100-ns-wide voltage pulse across the anode-cathode gap. This pulse is measured by a capacitive voltage probe, and a self-magnetic field current probe, which are located along the cathode shank, about 30 cm from the anode-cathode gap. It is important to remember that the measured voltage is not equal to the kinetic energy of the electrons. Although this would be true for a single electron, the situation is different for an intense electron beam. In the dense beam case, electrons will split their energy between kinetic energy and self-field energy. Thus, the space charge or self-field energy must be subtracted from the accelerating potential in order to determine the electron beam's kinetic energy.

From Gauss's law and the simple beam model shown in figure 11, the self-electric field can be written as

$$E_r = \frac{I_0}{2\pi\epsilon_0 v_z r} \qquad for \quad r_o > r > r_i, \tag{41}$$

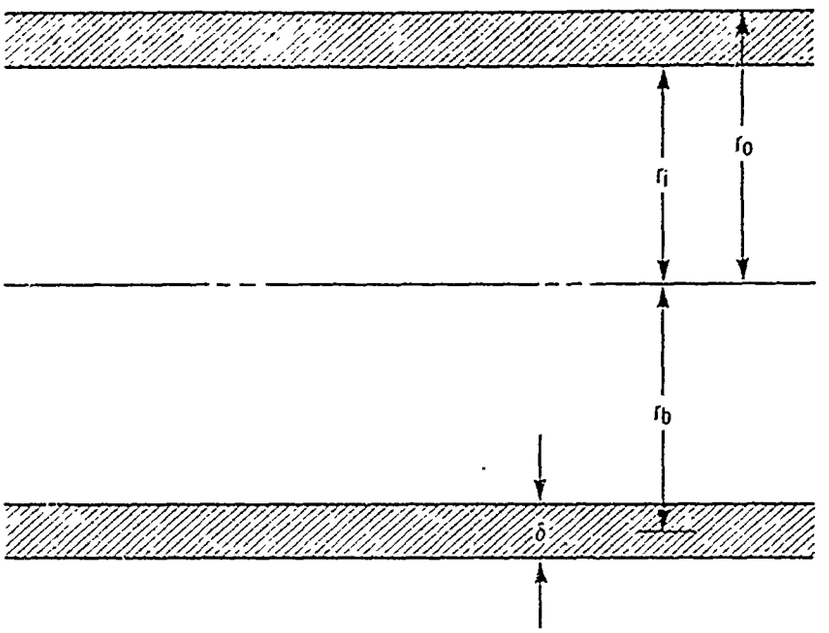

Figure 11. Idealized electron-beam geometry.

where I_0 is the beam current, v_z is the beam's axial velocity, ϵ_0 is the free space permittivity, and r is the radial measurement position. Note that $E_r = 0$ for $r < r_i$. Integrating E_r from the beam to the wall yields

$$\phi_{sc} = \frac{I_0}{2\pi\epsilon_0 v_z \ln(r_o/r_i)}, \tag{42}$$

where r_o and r_i are the radii of the wall and the beam. The conservation of energy gives

$$(\gamma - 1)mc^2 = (\gamma_0 - 1)mc^2 - e\phi_{sc}, \tag{43}$$

where $(\gamma - 1)mc^2$ is the kinetic energy of the beam, $(\gamma_0 - 1)mc^2$ is the accelerating potential, $e\phi_{sc}$ is the space charge energy, and γ is the standard relativistic factor $\gamma = (1 - \beta^2)^{-1/2}$.

For the experiments described in this report, the space charge depression represents the principal correction needed to extract the beam parameters γ and β from the accelerating potential. One should also note that the space charge depression is minimized when the beam propagates near the outer wall. Taking r_w equal to the average radius of the ripples in the slow-wave structure yields a correction of approximately 75 kV.

In order to analyze the FEL interaction and differentiate between FEL effects and those arising from cyclotron maser type interactions, the beam's perpendicular energy must be estimated. The principal source of this energy is the E × B drift [36] given by

$$v_\theta = \frac{E_r}{B_z}. \tag{44}$$

Here B_z represents the applied axial field and E_r is provided by either the angled electric field lines in the diode, the beam self-fields, or the E_r fields associated with the TM_{01} pump wave. For an applied field of 10 kG. and typical beam parameters, the E × B drift in the diode and from self-fields yields a maximum drift velocity of $\beta_\perp < 0.05$. From estimates of the electric field component of the TM_{01} wave [48], $\beta_{\theta_{max}} < 0.02$. An experimentally measured upper limit of $\beta_\perp < 0.05$ was obtained by methods more fully described in the diagnostic section.

3.3 The Backward Wave Oscillator Pump Wave

The backward wave oscillator (BWO) used in these experiments is a physically simple device in which an intense relativistic electron beam is passed through a rippled-wall type of slow-wave structure as shown in figure 12. The slow-wave structure interacts with the beam in such a way that some of the beam's kinetic energy is coupled into the propagating electromagnetic modes of the slow-wave structure. This is accomplished through the growth of negative-energy space charge waves on the beam. The mode, frequency, and intensity of the generated microwave radiation are determined by the geometry of the slow-wave structure, the electron beam, and the applied magnetic guide field.

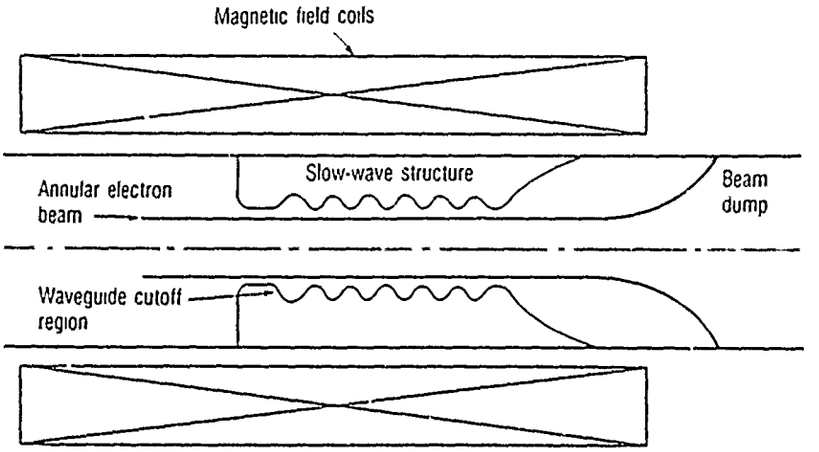

Figure 12. Rippled-wall slow-wave structure.

An important feature of BWO operation is the dependence of the power on the applied axial magnetic field. The characteristic field signature shown in figure 13 has been observed by several experimental teams [2, 31, 32, 49, 50]. The dip in the output power is due to the resonant reradiation into fast cyclotron waves on the electron beam [32].

Comparisons of the electromagnetic wiggler with its magnetostatic counterpart are facilitated by expressing the strength of the magnetic field component of the pump wave in gauss (G). A simple estimate is made by noting that the 50-MW, TM_{01} pump wave must flow through a corrugated-wall waveguide with $r_{min} \approx 0.5$ in. From the Poynting vector with sinusoidal time variation [36],

$$P_z/A = \frac{1}{2} Re(E_r \times H_\theta^*). \tag{45}$$

Assuming that P is constant over an area A and

$$|E_r| \approx \sqrt{\mu/\epsilon}|H_\theta| \tag{46}$$

with B = μH, one finds that

$$|B_w| = \left[\frac{2P\mu_0}{Ac}\right]^{1/2}. \tag{47}$$

For the above parameters, $B \approx 300$ G. A more detailed exposition of the BWO pump wave generator is found in appendix B.

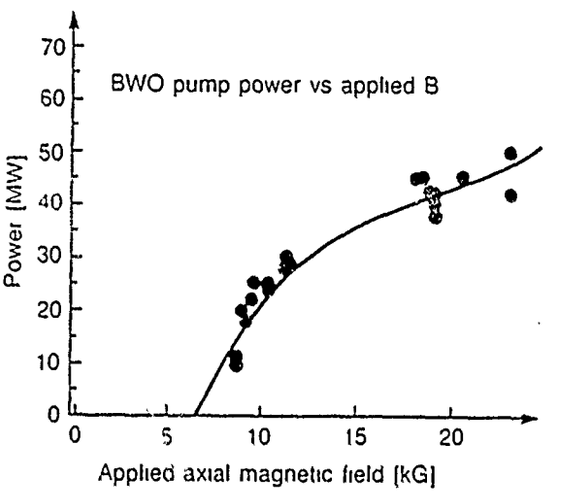

Figure 13. Plot of power versus applied magnetic field strength for BWO pump wave.

3.4 Support Systems

A background vacuum pressure of $\sim 1 \times 10^{-6}$ Torr was maintained in the beam propagation sections of the experiment by a standard 6-in. diffusion pump.

The field-emission diode and slow-wave structure are immersed in an applied axial magnetic guide field. A 1-m-long solenoid was used to produce fields up to 23 kG on axis. Energy for the coil was stored in a capacitor bank C, as shown in figure 14. When the capacitor bank was fully charged (and the Dragon pulser was also ready), switch S_1 was closed and coil L was energized. When the current in the coil reached its peak, the switch S_2 was closed--"crowbarring" the circuit. This gives the magnetic field more time to diffuse into the beam paths and prevents the system from "ringing" which decreases the lifetimes of the energy storage capacitors.

3.5 Diagnostics

The diagnostics used on this experiment fall into three basic categories: electron-beam diagnostics, microwave diagnostics, and support system diagnostics. This section focuses on the actual physical quantities that were measured and the parameters that can be inferred from them. Figure 15 shows the positions of the different diagnostics used in this experiment.

3.5.1 Beam Diagnostics

Information about the electron beam is provided by $\dot{D}$ and $\dot{B}$ probes that are located on the cathode stalk $\sim$30 cm from the anode-cathode gap. This places them just inside the magnetic guide field which helps to protect the capacitative $\dot{D}$ probe from stray electrons. The $\dot{D}$ and $\dot{B}$ probes are mounted on a 6-in. section of vacuum hardware that is shown in figure 16.

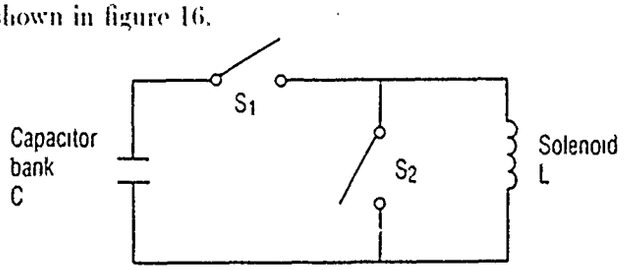

Figure 14. Schematic drawing of applied magnetic field system.

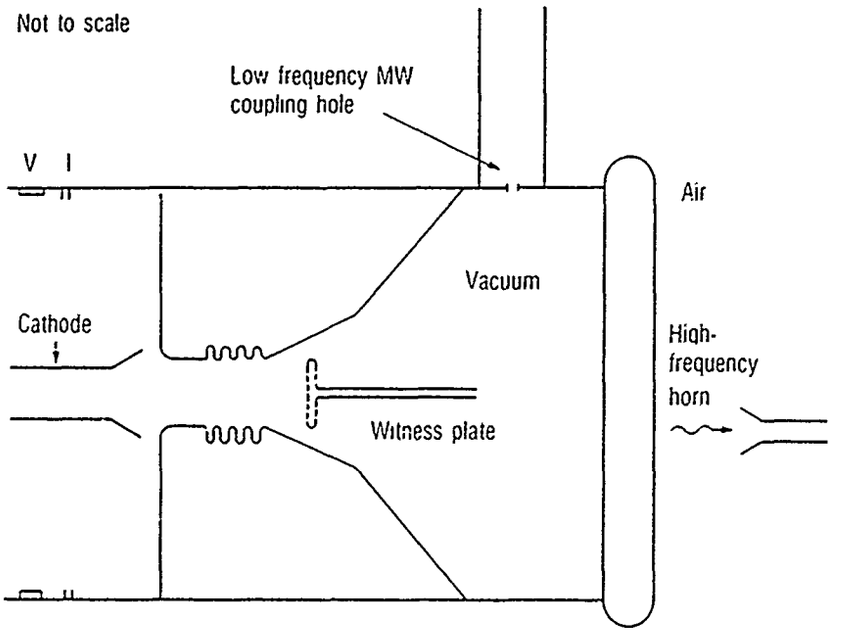

Figure 15. Diagnostic positioning on the EM-pumped FEL experiment.

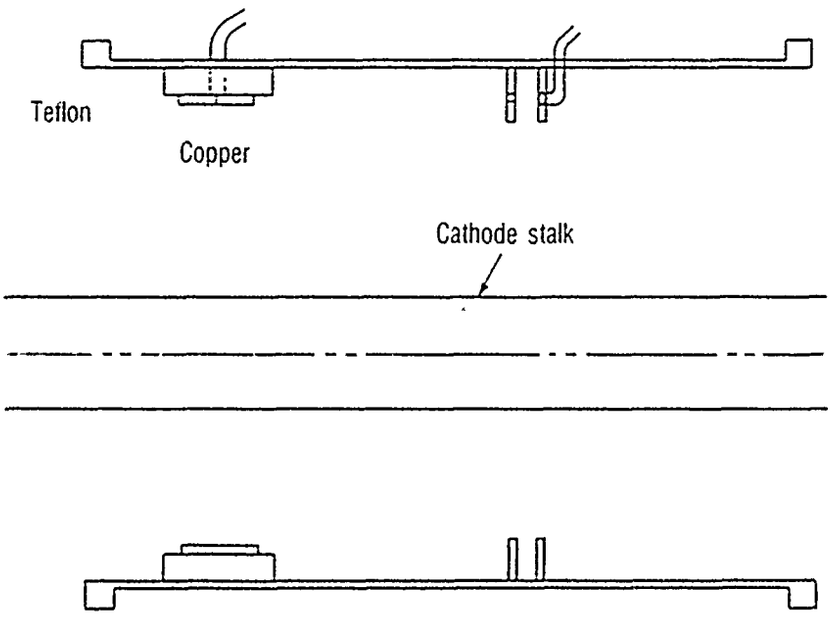

Figure 16. Detail of $\dot{D}$ and $\dot{B}$ electron-beam voltage and current probes.

The $\dot{D}$ probe is a cylindrical capacitive divider whose output is proportional to the time derivative of the voltage pulse traveling down the transmission line formed by the cathode stalk and the 6-in. outer diameter (OD) vacuum hardware. The pickoff is a thin, 1-in.-wide piece of copper tape insulated from the vacuum wall by a 0.125-in.-thick piece of Teflon. The copper tape is "terminated" in 10 Ω by four 50-Ω resistors and the 50-Ω signal cable that are evenly spaced around the circumference of the cylinder. The signal is then fed into a passive analog integrator and stored on a computer disk via a fast signal digitizer. Careful calibration of the probe yielded a sensitivity of 477 kV per volt of input when the probe was connected to an integrator with a 3-μs time constant.

The current probe, which is also shown in figure 16, consists of a small loop which is aligned to intercept the self-B_θ of the current flowing down the cathode stalk. The probe is formed by breaking the continuity of the loop, then connecting a piece of coaxial cable across the "break." Since the voltage induced into the cable is proportional to the time derivative of the current, the output of this probe must also be integrated. Careful calibration of this probe yielded a sensitivity of 7.9 kA/V when the probe was operated into a 3-μs integrator. Some typical voltage and current traces are shown in figure 17.

More information about the beam can also be obtained by examination of witness plates that were placed as shown in figure 15. The time-integrated position of the beam is etched directly on the plates. Typical values for these experiments were a beam inner diameter (ID) of 1.65 cm and an OD of 1.85 cm. The width of the beam fixes an upper limit on the amount of perpendicular energy possessed by the beam. An electron with transverse energy will gyrate in the applied magnetic field with a gyroradius given by

$$r_g = \frac{\beta_\perp c}{\Omega_0/\gamma}, \tag{48}$$

where Ω_0 is the nonrelativistic electron cyclotron frequency. As indicated in figure 18, the maximum value for r_g is one-half the beam thickness or ~1 mm. For an applied magnetic field of 10 kG and $\gamma = 1.9$, equation (48) yields a maximum value for $\beta_\perp$ of ≈0.05. A photograph of one of the actual targets is shown in figure 17. In principle, one could also consider the beam a rigid rotor. In this case $r_g \sim 0.9$ cm (max) and equation (48) yields a value of 0.45 for $\beta_\perp$!

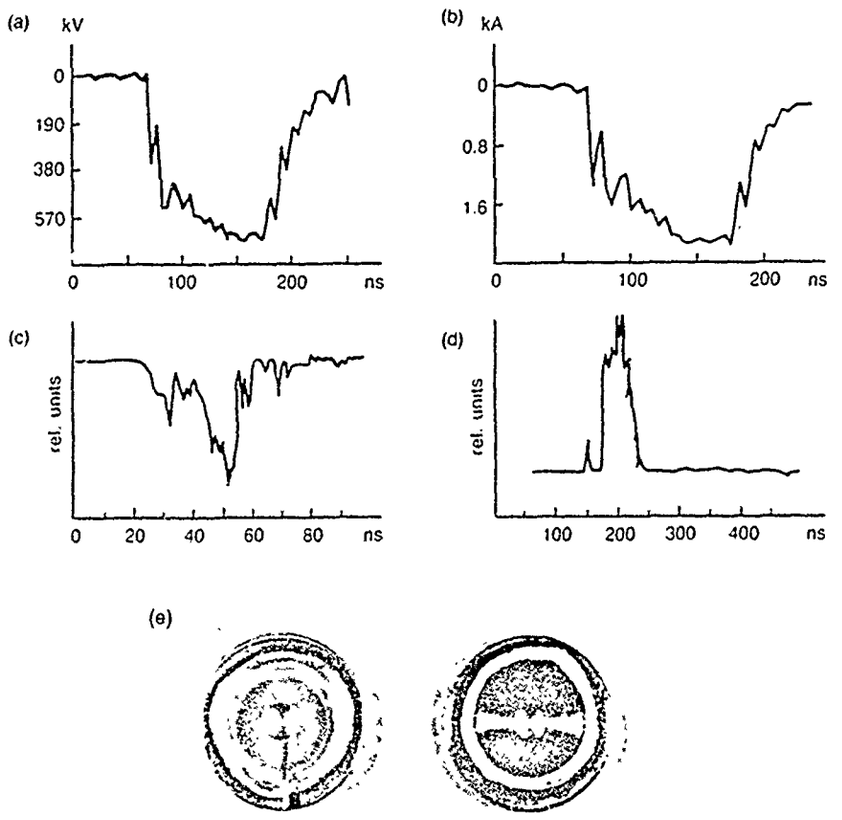

Figure 17. Typical experimental data showing (a) voltage, (b) current, (c) BWO pump wave, (d) high-frequency radiation, and (e) witness plate.

3.5.2 *Microwave Diagnostics*

In these experiments, high-power microwave radiation was measured in the frequency ranges from 7 to 18 GHz and from 50 to 130 GHz. Microwaves in the low range (7 to 18 GHz) were studied via the coupling hole shown in figure 15 while the high range was collected with the horn—also shown in figure 15.

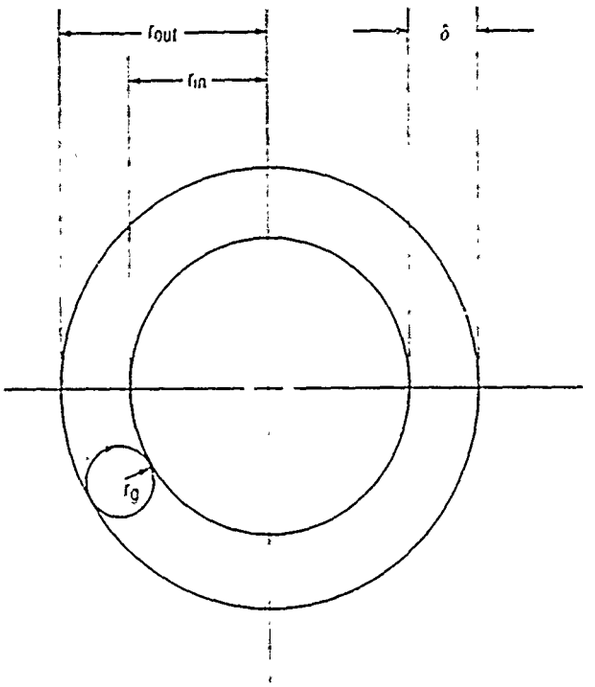

Figure 18. Idealized electron beam cross section.

The detection methods for the low-frequency microwaves are illustrated in figure 19. A small aperture in the side of the vacuum cylinder allows some of the high-power microwave radiation to enter a section of WR-90 (X-band) rectangular waveguide which carries the signal to the rf-shielded data collection room. A 20-dB waveguide directional coupler then splits part of the signal into a "prompt" path and a section of coiled dispersive waveguide. Waveguide-to-coaxial adapters were used to bring both the prompt and dispersed signals into coaxial cable. Coaxial couplers were then used to further split the signals for analysis.

An array of bandpass and low-pass filters was used to isolate and study different portions of the frequency spectrum from 7 to 12.4 GHz. Higher frequency high-pass filters were constructed with sections of WR-62 waveguide (f_c = 9.486 GHz) and WR-42 waveguide (f_c = 14.047 GHz). The WR-90 waveguide has a cutoff frequency of 6.557 GHz. The filters were especially useful for identifying peaks in the dispersed signals.

In addition to the standard dispersion line and filter techniques, microwave mixers [51] were also used to study the frequency spectrum of the observed radiation. As indicated in figure 19, a known, convenient

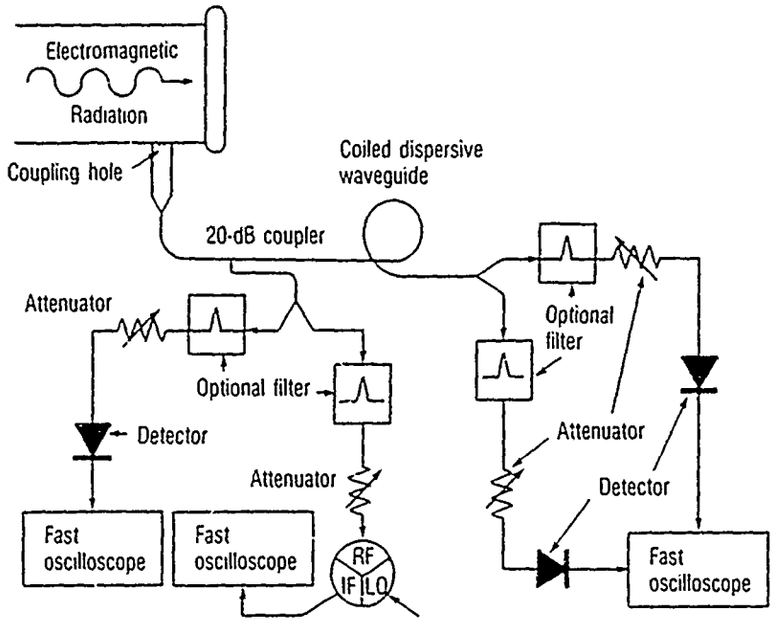

Figure 19. Schematic drawing of low-frequency high-power microwave diagnostic system.

frequency is applied to the local oscillator (LO) input, and the difference frequency between the LO and rf appears at the intermediate frequency (IF) port and is recorded directly on a fast oscilloscope. By changing the LO and observing the corresponding change in the IF, one can accurately determine the rf input frequency—especially if one is able to Fourier analyze the IF signal.

All waveguide runs and components were easily calibrated from 7 to 18 GHz with a network analyzer system. The coupling holes that fed the WR-90 waveguide could not be calibrated by such simple means. Since the hole coupling is highly mode sensitive, a TM_{01} mode launcher was constructed [52]. The need to physically tune the mode launcher restricted the range of frequencies over which it could be swept. However, excellent data were obtained near 8.4 GHz, the operating frequency of the BWO pump wave.

Measurements of the high-frequency microwave spectrum were made from 50 to 130 GHz. For these measurements, a small horn (area ~0.88 cm^2) was placed just behind (~25 cm away) the polyethylene window that provided the vacuum-to-air interface in the experiment. The out-

put of the horn was fed into the microwave grating spectrometer [53] which acts like a bandpass filter. By changing the grating angle and using different gratings, it was possible to study "frequency windows" from 50 to 130 GHz. Crystal detectors were mounted directly on the spectrometer, and their detected output was fed back to the shielded data room where it was recorded on a fast oscilloscope. Some typical traces for the BWO pump wave and the high-frequency radiation are shown in figure 17. The spectrometer is described in more detail in appendix C.

3.5.3 *Support System Diagnostics*

In addition to such obvious parameters as vacuum pressure and machine charging voltage, two other electrical signals are routinely recorded on each shot: magnetic field and the voltage on the Dragon machine's charge line.

A single-loop pickup coil located just outside the vacuum cylinder near the diode is used to generate a signal proportional to the time derivative of the applied magnetic guide field. This signal is fed into a digitizer and integrated numerically. A small correction factor is applied to account for the diffusion time of the magnetic field into the region traversed by the electron beam.

The charge line voltage is monitored by a self-integrating $\dot{D}$ probe [54] that is also fed into a digitizer in the computer data acquisition system.

3.6 Experimental Operation

Before the experiment described in this report began, the Dragon machine was tuned to provide relatively flat voltage and current pulses. Although some minor re-tuning was required in the later stages of the experiment, the voltage and current traces were very reproducible throughout the experiment. Despite considerable variation in signal amplitude (factors of 2 to 5 were not uncommon) on a shot-to-shot basis, the positions of the frequency peaks were quite reproducible—to $\approx$1.5 GHz, the resolving power of the spectrometer. In fact, the general experimental procedure was to scan frequency ranges from low to high and then back to low to ensure that the frequency peaks were reproducible. It was also possible to reproduce the same peaks on a day-to-day basis.

Studies were also conducted on the magnetic field system [55] to ensure that the field emission diode and the slow-wave structure would reside in the flat-field region of the solenoid. These studies also quantified the relation between the field monitor pickup loop outside the vacuum cylinder and the actual field inside the slow-wave structure. Shot-to-shot reproducibility of the magnetic field system was excellent; the only problems came from the transient digitizers that were used to record the data signals. Frequent air-conditioning problems and a hotter than normal summer often resulted in equipment overheating which caused baselines to drift, affecting the integration of the $\dot{B}$ magnetic field monitor.

The stainless-steel cathode and carbon anode were periodically inspected, but no damage or significant deterioration was evident. The anode and cathode were approximately 2000 shots "old" by the conclusion of the experimental period.

Four Tektronix 7612 transient digitizers [56] were used to record the magnetic field signal, the voltage on the Dragon charge line, and the voltage and current on the cathode stalk. A DEC PDP-11/34 computer was then used to store the data on removable disk cartridges and finally on tape. This system allowed convenient examination and later storage of the slower data signals without the costs and troubles of recording them on film.

Three Tektronix 7104 oscilloscopes (1-GHz bandwidth) [56] were used to record the faster microwave signals. This limited the amount of data that could be recorded on any given shot but still provided enough flexibility so that the lower frequency (7 to 20 GHz) signals could be thoroughly studied.

The high-power-microwave output from the experiment leaves the vacuum cylinder (after passing the coupling hole) by passing through a polyethylene window and then into a mini anechoic chamber. After approximately 1500 microwave shots, some discoloration is evident on the polyethylene window, but it does not appear to have had any significant impact on the experiment. The mini anechoic chamber not only eliminates any safety problems that might be caused by high levels of nonionizing radiation, but also reduces the noise level at the high-frequency spectrometer.

4. Results and Discussion

4.1 Introduction

The high-frequency spectrum from 50 to 130 GHz is composed of an array of regularly spaced peaks. The frequencies of the peaks and their variation with the strength of the axial magnetic guide field indicate that the spectrum is due to a three-wave FEL interaction in which cyclotron harmonic beam waves act as "idlers." A detailed examination of low-frequency, low-harmonic-number data will be used to demonstrate that the emission spectrum is due to an FEL interaction and not to a CHARM interaction. This is important because of the close similarity between the FEL and CHARM spectra—especially at high frequencies

The raw data are presented in the next section, followed by a comparison of the data with the model of an electromagnetically pumped FEL with cyclotron harmonic idlers. The last sections provide a more complete justification for choosing the FEL rather than the CHARM as the interaction model that best describes the experimental results.

4.2 The Measured High-Frequency Spectrum

The experimental procedure was to select a value for the magnetic guide field, and then use the grating spectrometer to sweep through the frequency range appropriate to the particular grating and detector. This process yielded tables of power versus frequency for different values of applied magnetic field. The electron-beam parameters were held constant throughout the experiment. Some typical power spectra are shown in figures 20 through 22.

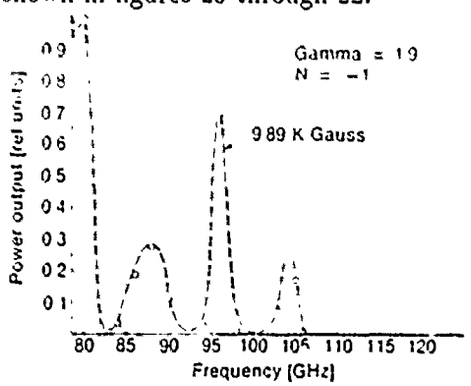

Figure 20. Measured frequency spectrum from 80 to 120 GHz for an applied field of 9.89 kG.

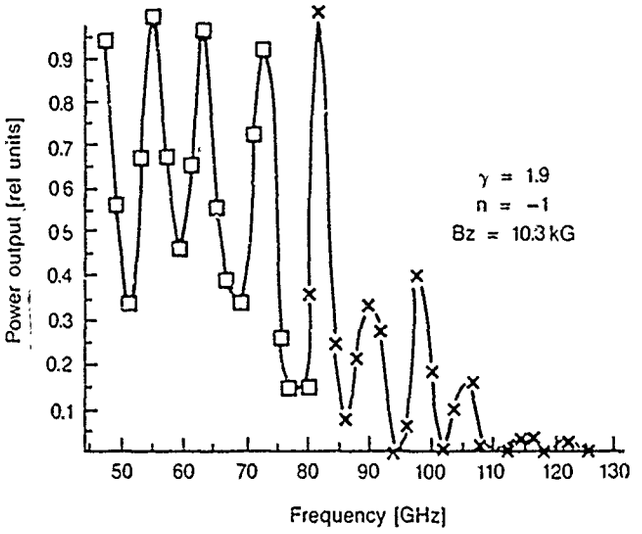

Figure 21. Measured frequency spectrum from 50 to 125 GHz for an applied field of 10.3 kG.

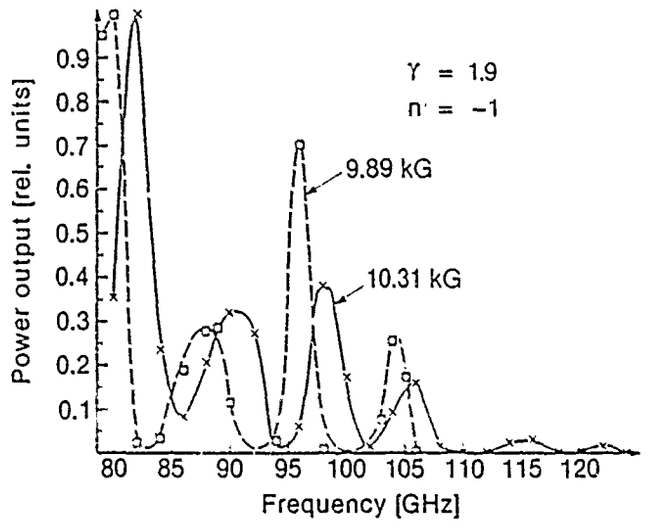

Figure 22. Measured frequency spectra from 80 to 125 GHz for applied fields of 9.89 and 10.3 kG showing frequency shift caused by a change in applied field.

Figure 20 shows the simple set of regularly spaced peaks present between 80 and 120 GHz for an applied magnetic field of 9.89 kG. The data have been normalized to the highest peak present in the frequency range.

In figure 21, two measured spectra have been joined together. Although the same magnitude of magnetic field was applied in both cases, different gratings and detectors were required to cover the two contiguous frequency ranges. Also, both data sets were normalized separately. This is the reason for the "hump" in relative magnitude at approximately 82 GHz. In general, the power decreases monotonically as the frequency increases.

In figure 22 the spectra corresponding to two different values of magnetic field are plotted on the same axes. It can be clearly seen that the entire frequency spectrum is shifted when the magnitude of the guide field is changed. The data sets were normalized separately even though the same diagnostic components were used in both cases. Although not shown in this section, spectra were also measured for several other values of the magnetic field, including 11.4, 19.4, and 20.3 kG. Regularly spaced peaks were always present.

4.3 The EM-Pumped FEL Model

In this section the experimental data are compared to the theoretical model of the electromagnetically pumped FEL with cyclotron harmonic idlers that was developed in the last section.

4.3.1 Expected Spectrum

The frequency spectrum was expressed in section 2 by equation (37). For the data presented in the previous section, the minimum frequency was 50 GHz and waveguide effects can be ignored. Equation (37) can then be reduced and cast in terms of frequencies to become

$$f_s = \gamma_{\parallel}^2 \left[f_w \left(1 + \frac{\beta_{\parallel}}{\beta_{ph}}\right) + \ell f_{ce} \right] (1 \pm \beta_{\parallel}), \tag{49}$$

where f_s and f_w are the frequencies of the scattered and pump waves and f_{ce} is the relativistic electron cyclotron frequency.

The dispersion diagram for the model is shown in figure 23. Note that the interaction sites of interest lie along the "down shifted" branch.

The lines representing the different resonance conditions for each harmonic (labeled $\ell = 1$ through 12) will move up and down as the magnetic field, and hence f_{ce}, is changed. Recall in equation (49) that a positive value for β_{ph} represents a backward propagating wave. The spacing of the frequency peaks indicates that the down-shifted branch will best match the experimental data; thus the minus sign must be favored in the last factor. The formula for the frequency peaks as a function of magnetic guide field is then

$$f_s = \gamma_{||}^2 \left[f_w (1 + \frac{\beta_{||}}{\beta_{ph}}) + \ell f_{ce} \right] (1 - \beta_{||}). \qquad (50)$$

The following parameters were used in the above expression:
$\gamma_{||} \sim 1.9$,
$\beta_{||} \sim 0.85$,
$f_w \sim 8.4$ GHz ,
$\beta_{ph} \sim 1.054$,
and of course f_{ce} is $2.8/\gamma_{||}$ (GHz/kG).

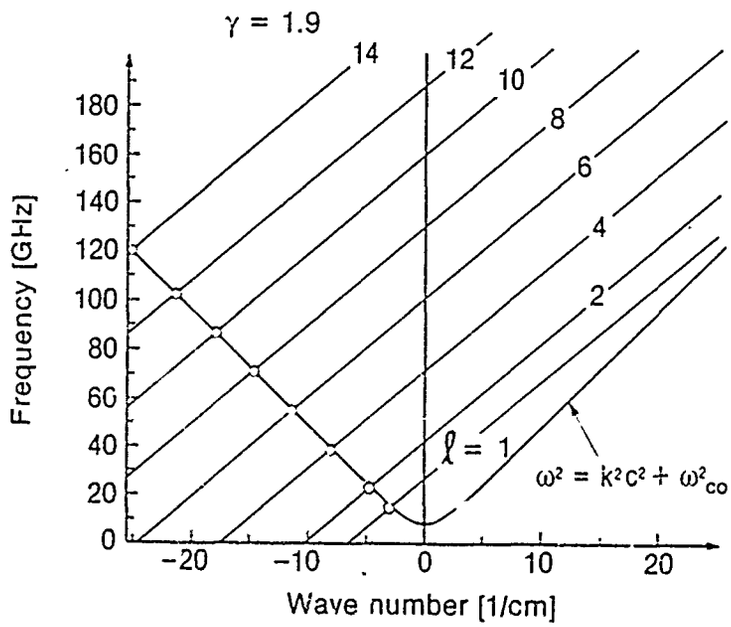

Figure 23. Dispersion diagram for EM-pumped FEL with cyclotron harmonic idlers with theoretical intersection points marked with circles.

It should be noted that equation (50) can also be reached directly via the appropriate Stokes diagram shown in figure 24 and the conservation equations. From the conservation of energy,

$$\omega_w = \omega_i + \omega_s, \tag{51}$$

and from the conservation of momentum,

$$\mathrm{k}_w = \mathrm{k}_i + \mathrm{k}_s. \tag{52}$$

The dispersion relation of a slow, negative-energy cyclotron harmonic wave is given by

$$\omega_i = \mathrm{k}_i \cdot \mathrm{v} - \ell\Omega_0. \tag{53}$$

For $\mathrm{v} = v_\parallel \hat{z}$, equations (53) and (51) may be combined to yield the relation

$$\omega_s = \omega_w - \mathrm{k}_i \cdot \mathrm{v} + \ell\Omega_0 \tag{54}$$

or

$$\omega_s = \omega_w - (\mathrm{k}_w - \mathrm{k}_s)\cdot\mathrm{v} + \ell\Omega_0. \tag{55}$$

However, from the Stokes diagram in figure 24, both the pump wave and the down-shifted branch of the scattered radiation are backward propagating. Thus, equation (55) becomes

$$\omega_s = \omega_w + (k_w - k_s)v_\parallel + \ell\Omega_0, \tag{56}$$

where $k_s \approx \omega_s/c$ and $k_w = \omega_w/v_{ph}$. Substituting for k_s and k_w leads to

$$\omega_s(1 + \beta_\parallel) = \omega_w(1 + \beta_\parallel/\beta_{ph}) + \ell\Omega_0, \tag{57}$$

or

$$\omega_s = \gamma^2\left[\omega_w\left(1 + \frac{\beta_\parallel}{\beta_{ph}}\right) + \ell\Omega_0\right](1 - \beta_\parallel), \tag{58}$$

which is identical to equation (50).

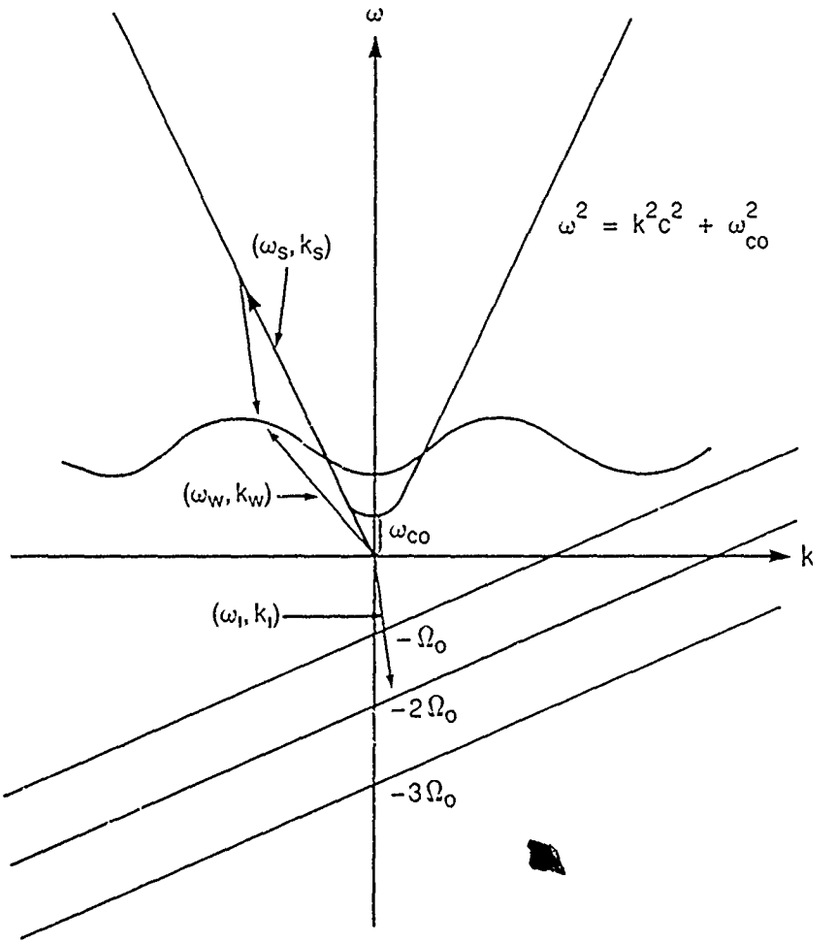

Figure 24. Stokes diagram of three-wave FEL interaction with backward propagating pump wave, slow cyclotron harmonic wave idler, and scattered radiation along "down-shifted" branch.

5.3.2 Comparison of Theory and Experiment

The excellent match between the experimental data and the predictions of the simple model represented by equation (50) is shown graphically in figures 25 and 26. In these figures, crosses are used to denote the positions of the measured peaks on the theoretical scales. The even and odd harmonics were plotted separately to prevent crowding on the graphs.

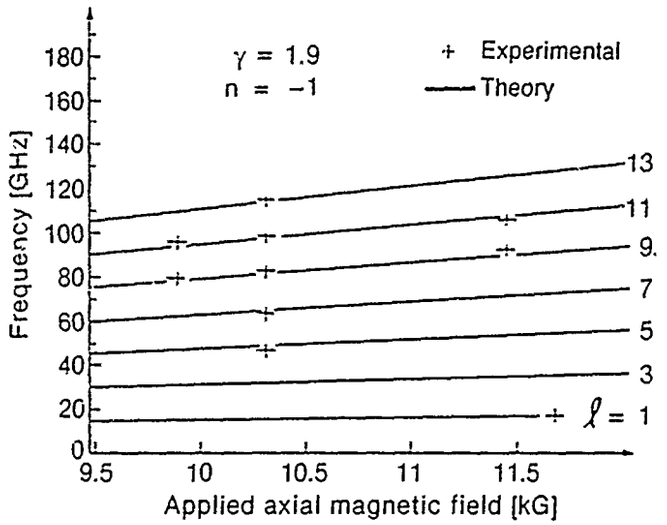

Figure 25. Dependence of frequency peaks on magnetic field for odd harmonic numbers from 1 through 15 with crosses marking positions of measured peaks.

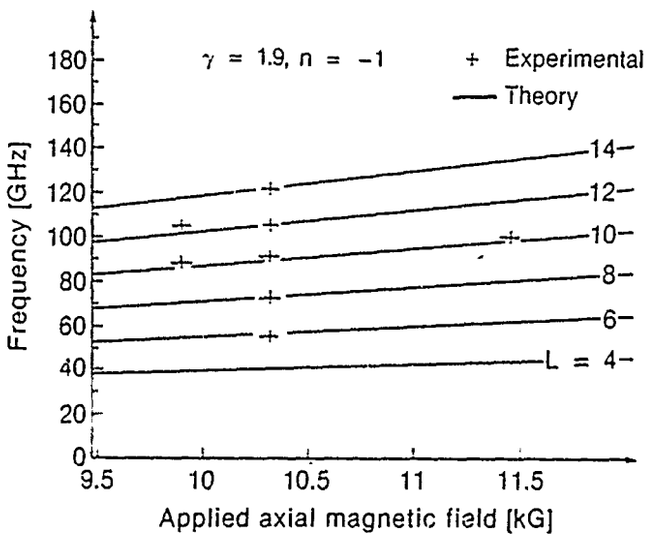

Figure 26. Dependence of frequency peaks on magnetic field for even harmonic numbers 4 through 14 with crosses marking positions of measured peaks.

The two most convincing aspects of the fit between theory and experiment are the peak spacing and magnetic field dependence. Peaks representing harmonic numbers $\ell = 1$ and $\ell = 5$ through 14 can be clearly identified on the figures. Data showing the change in frequency corresponding to changes in the applied magnetic guide field also fit well into both figures 25 and 26. This variation in frequency with magnetic guide field is especially important because it not only eliminates several prospective mechanisms for high-frequency-microwave production but also eliminates the possibility that the peaks were due to resonances in the diagnostic system.

4.3.3 *Power Estimates*

For the high frequencies, the signal strength times the detector sensitivity times the in-line attenuation yields a level for the peak power entering the pickup horn (shown in fig. 15 and 27) that feeds the grating spectrometer and hence the rest of the high-frequency detection system. For the $\ell = 9$ peak at 82 GHz, this calculation gives a result of approximately 20 W at the pickup horn (0.9-cm^2 cross-sectional area). Although this is a very small fraction of the total power (at 82 GHz) produced in the experiment, realistic measurements would require mode and radiation pattern information that is beyond the scope of this report. However, a crude estimate can be made by considering the idealized model shown in figure 27. Here the actual radiation source in the cylindrical waveguide has been replaced by a "point source" located at the center of the end of the guide. This yields a geometric attenuation factor of ~4400, which would imply a power of ~90 kW in the waveguide (at 82 GHz). This estimate could be considerably higher or lower, depending on the actual radiation pattern.

The low-frequency measurements were based on energy coupled through a hole in the side of the cylindrical waveguide, as discussed in section 3.5.2. For the 8.1-GHz pump wave, unambiguous power levels of 50 MW were routinely measured. However, the other "low" frequency peak occurred at ~16.5 GHz. In this case, mode uncertainty precludes any simple estimate of the power. The best guess is to assume that power drops by ~10 to 15 percent each time the mode number is increased. Then working back from the high-frequency estimate at 82 GHz ($\ell = 9$), one can crudely determine that 200 to 300 kW should be found at 16.5 GHz for the $\ell = 1$ harmonic.

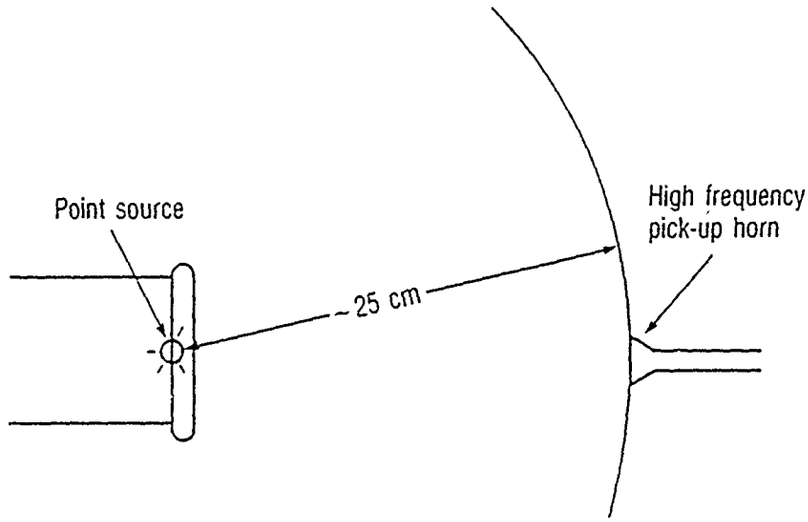

Figure 27. Illustration of model used to construct crude estimate of high-frequency microwave power levels.

4.4 Other Models

Although the experimental data clearly fit the down-shifted branch of the backward wave electromagnetically pumped FEL model, it must also be shown that other competing theories are inappropriate. The principal contenders are the forward pump wave FEL interaction and the CHARM. Models based on the excitation of higher order modes in the BWO can easily be dismissed by considering the experimental frequency shift versus magnetic field. The high-order BWO modes are solely a function of the geometry and do not depend on applied magnetic field strength. In the next sections, the possibility of a forward pump wave interaction or a CHARM is considered in more detail.

4.4.1 Forward Pump Wave FEL Interaction

The operation of the experiment is such that the "normal" backward propagating pump wave passes through the slow-wave structure (as in fig. 10), reflects from a section of waveguide beyond cutoff, and again passes through the slow-wave structure—this time moving with the electron beam. Clearly, an interaction is theoretically possible, and the spectra can be computed from equation (37) or (49) with $\beta_{ph} \rightarrow -\beta_{ph}$.

Although equation (37) will be used in all calculations (because waveguide effects may not always be ignorable), equation (49) is easier to "look at" and it contains the same basic physics—except for the waveguide effects. Table 1 contains the up- and down-shifted interaction frequencies for both forward and backward pump waves. Clearly, the measured spectra are not due to any interaction based on the up-shifted branch of either the forward or backward pump waves. As a result, only the down-shifted branches will be considered from this point onward.

Table 1. Interaction frequencies (in gigahertz) of an electromagnetically pumped FEL with cyclotron harmonic idlers for an applied field of 10 kG

l	Backward pump up-shifted	Backward pump down-shifted	Forward pump up-shifted	Forward pump down-shifted
1	199.0	17.0	107.7	10.4
2	297.7	24.7	206.9	17.6
3	396.3	32.5	305.6	25.3
4	494.8	40.4	404.2	33.2
5	593 3	48.3	502.7	41.0
6	691.8	56.2	601.2	48.9
7	790.2	64.2	699.7	56.9
8	888.7	72.1	798.1	64.8
9	987.1	80.1	896.6	72.2
10	1085	88.0	995.0	80.7
11	1184	96.0	1093	88.6
12	1282	103.9	1192	96.6
13	1381	111.9	1290	104.5
14	1479	119.8	1389	112.5
15	1578	127.8	1487	120.5

At high frequencies ($\ell > 4$), the spacing between the peaks and the magnetic field dependence is virtually identical for both the forward and backward pump waves - when viewed locally. When data are taken in a wide range of magnetic field, identifying the peaks with specific mode numbers becomes very difficult. This is complicated by the fact that even though the harmonic numbers are different, the forward and backward pump models predict almost identical spectra. However, the situation is significantly different at lower frequencies ($\ell < 3$). The forward wave model predicts interactions at both 10.4 and 17.6 GHz, while the backward wave model predicts only a single interaction at 17 GHz. Careful study of the frequency range from 7 to 20 GHz revealed peaks at only 8.4 GHz (the pump frequency) and 16.5 GHz. There was no microwave power detected in the frequency range near 10.4 GHz. A graphical representation of the low harmonic interaction frequencies is

given in figure 28, where the lone experimentally observed frequency is denoted by the circled cross. The $\ell = 0$ (no idler) interaction was also absent.

In addition, there was no clear evidence of the three-wave FEL with space charge idler that was briefly discussed in section 2.2. The interaction frequency for the down-shifted branch was ~6.5 GHz, which is below the cutoff frequency of the waveguide used to transport the microwave signals and it was therefore not detectable. The up-shifted interaction frequency should have produced a peak at ~80 GHz that would not change with the applied magnetic field, but no such peak was observed in the hf spectrum. Thus, the electromagnetically pumped FEL with space charge idlers did not produce observable power in these experiments.

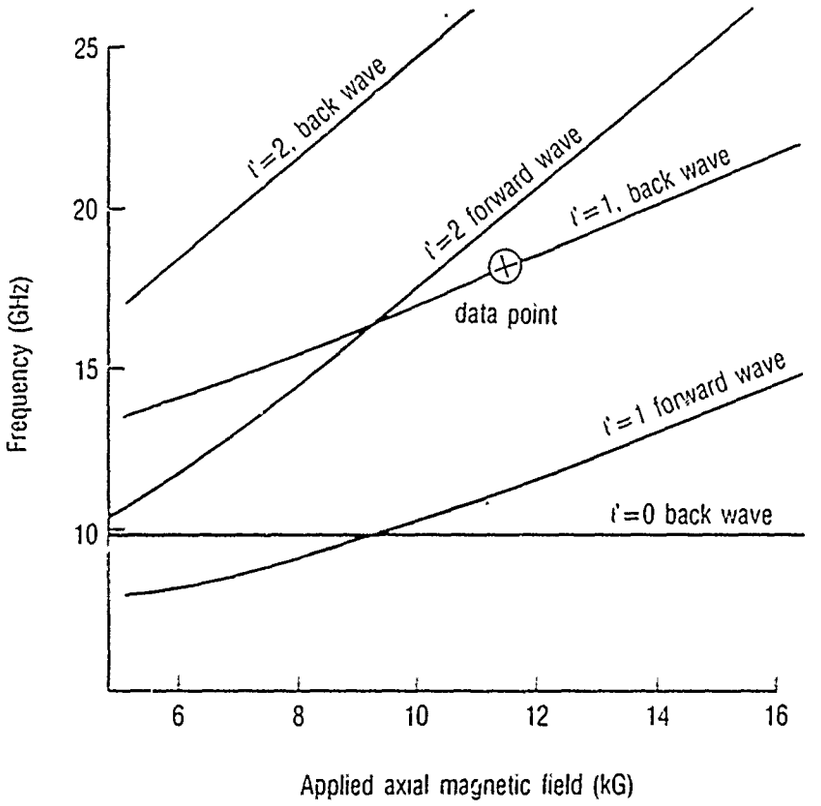

Figure 28. Low-harmonic interaction frequencies versus applied magnetic field for down-shifted branches of EM-pumped FEL with cyclotron harmonic idler waves.

4.4.2 *The CHARM Model*

The expected frequency spectrum from a CHARM interaction was shown in section 2.3 to be given by equation (40). Table 2 shows some interaction frequencies predicted by equation (40) with similar frequencies representing the down-shifted backward EM-pumped FEL interaction. Once again, the down-shifted branch of the CHARM interaction predicts a high-frequency spectrum quite similar to that of the FEL. In fact, figure 29 shows the measured data on a plot of the interaction frequencies generated by the CHARM model via equation (40). However, there are once again significant differences in the low frequency ($\ell < 3$) spectrum. These differences are clearly seen in figure 30 in which the down-shifted spectra are plotted for the CHARM and backward pump wave FEL interaction. The solid lines represent theory and the crosses denote experimentally measured peaks. A careful search of the microwave spectrum was able to detect power only at the single frequency marked by the circled cross. The CHARM model fails to adequately predict the measured frequency spectrum.

Table 2. Interaction frequencies (in gigahertz) for a cyclotron harmonic auto-resonant maser with an applied field of 10 kG

Harmonic l	CHARM up-shifted	CHARM down-shifted
1	94	12.5
2	195	18.1
3	294	25.3
4	393	32.9
5	491	40.7
6	590	48.5
7	688	56.4
8	787	64.3
9	886	72.2
10	984	80.1
11	1082	88.0
12	1181	95.9
13	1279	103.9
14	1378	111.8
15	1476	119.8

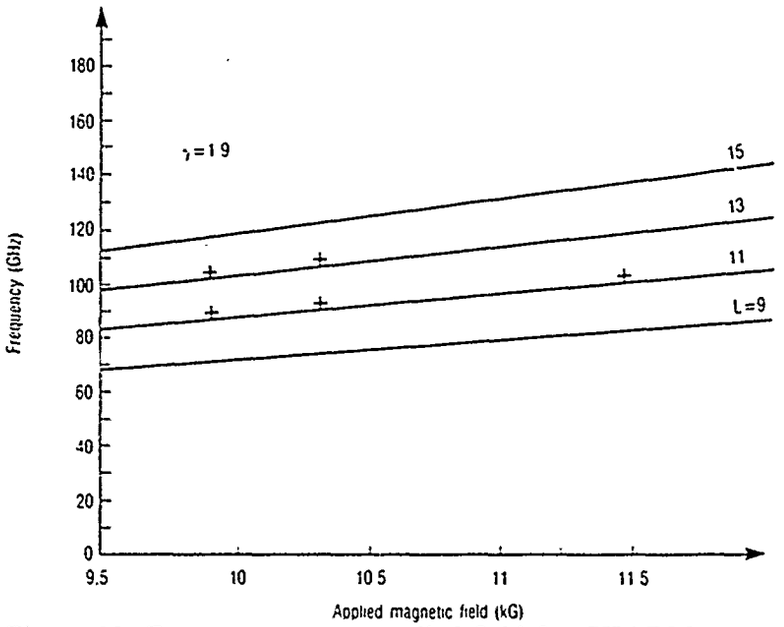

Figure 29. Frequency versus applied field for CHARM interaction with experimental data points represented by crosses.

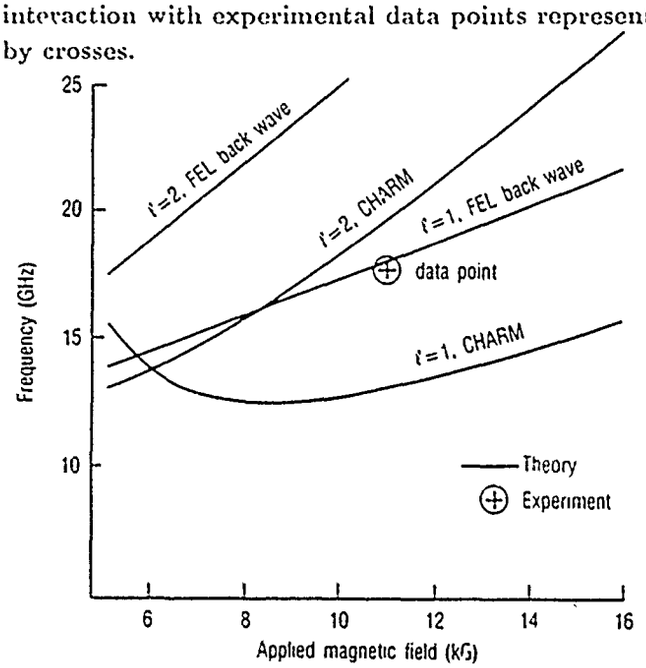

Figure 30. Low-harmonic interaction frequencies versus applied magnetic field for down-shifted branches of CHARM and EM-pumped FEL with backward pump wave and cyclotron harmonic idlers.

In addition to the poor match between low-frequency predictions and experimental measurements, the CHARM model is inappropriate for another reason—insufficient $\beta_\perp$. In order to drive the CHARM instability, a large amount of perpendicular energy is required in the electron beam. In fact, the resonance point occurs when $\beta_\perp = 1/\gamma$ [45, 46]. For the parameters of this experiment, $\beta_\perp \sim 0.5$ would be required. However, the witness plate measurements of the electron beam (sect. 3.5.1) showed a measured value of $\beta_\perp < 0.05$, which is much less than the perpendicular energy needed to efficiently drive the CHARM interaction.

In a pure CHARM device, there are no rippled walls. The interaction is driven by $\beta_\perp$ and the applied magnetic field. When a thin foil was inserted into the slow-wave structure (effectively eliminating the corrugations), all microwave radiation ceased—both high and low frequency. This supports the assertion that the observed microwave spectrum was due to a non-CHARM type of process. Thus, all evidence points to the backward-wave electromagnetically pumped FEL with cyclotron harmonic idlers as the model that best explains the measured data.

4.5 Frequency Scaling

An interesting feature of this novel FEL mechanism is its frequency scaling with γ, as shown in figure 31. Also shown in the figure are the up-shifted (+) and down-shifted (−) frequency conversion factors for magnetostatically (labeled SM) and electromagnetically (labeled EM) pumped FEL's with space charge wave idlers. Note that the behavior predicted for a down-shifted electromagnetically pumped FEL with a cyclotron harmonic idler (labeled CI in fig. 31) is dramatically different from the behavior of the other FEL mechanisms since the output frequency decreases with increasing γ. The figure shows the specific scaling law for harmonic number $\ell = 10$, but the behavior is typical for all harmonic numbers. It can easily be understood by referring to equation (49). There Ω_0 is the relativistic electron cyclotron frequency which decreases with increasing γ, and the term ℓf_{ce} is dominant. Recall that $\gamma^2(1 - \beta_\parallel) = (1 + \beta_\parallel)^{-1} \approx 2$. Note also that it is possible to tune the frequency of the FEL by varying either the axial magnetic guide field or γ.

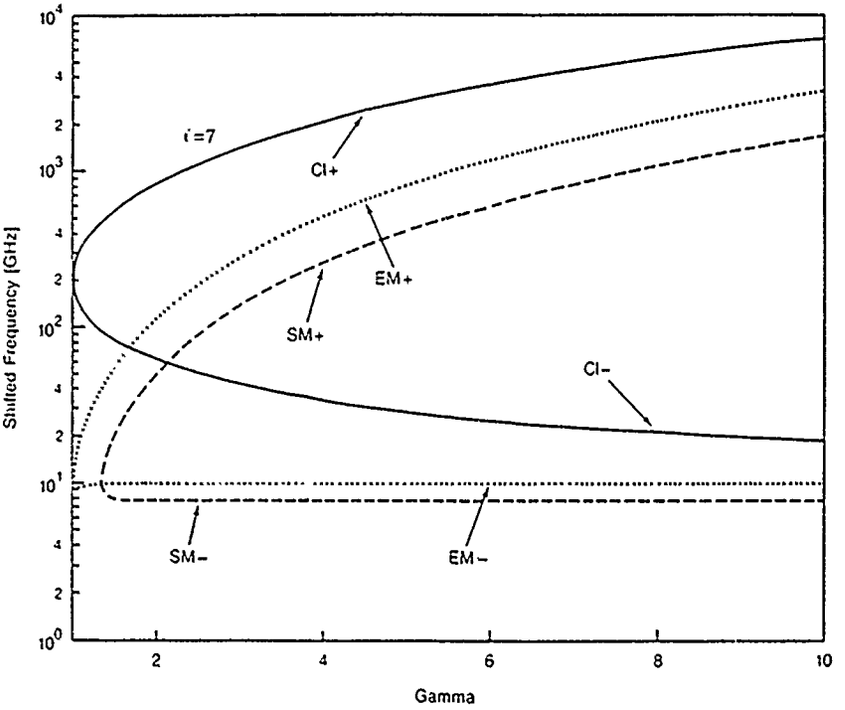

Figure 31. Plot of frequency versus gamma for several interaction models.

5. Conclusions

Although the concept of using an electromagnetic wave to pump a FEL type of interaction has been demonstrated previously [1, 2, 20, 44], the experiments discussed in this report represent the first careful study of a significant portion of the frequency spectrum produced by such devices. In fact, the spectrum was resolved from 7 to 20 GHz and from 50 to 130 GHz. Quite unexpectedly, the spectrum was found to be composed of an array of regularly spaced peaks.

Several interaction mechanisms were used to model the experimentally measured frequency spectrum. The most successful were the down-shifted branches of the CHARM and FEL with cyclotron harmonic idlers. The CHARM model was dismissed because it did not adequately predict the low-frequency portion of the spectrum and the beam did not appear to possess a sufficient amount of perpendicular energy. The lone remaining candidate model was the electromagnetically pumped FEL with cyclotron harmonic idlers.

A three-wave FEL interaction with a cyclotron idler wave has been reported [41-43], but the experiments reported here represent the first time that cyclotron harmonic idler waves have been observed. The actual implementation of the experiment allowed both forward and backward waves to interact with the electron beam. Optimistically, this provided the opportunity to study both the forward and backward interactions. Fortunately, the differences in the spectra predicted by the two models were sufficiently distinct so that the forward pump wave model could be eliminated in favor of the backward-wave-driven interaction. Thus, it has been demonstrated that backward electromagnetic wave pumping in the presence of an axial magnetic guide field produced a three-wave FEL interaction via cyclotron harmonic idler waves.

The production of this coherent, powerful, high-frequency microwave radiation was achieved with relatively modest magnetic-field and electron-beam parameters. This FEL mechanism also features continuous tunability by varying either the applied magnetic guide field or γ.

At the point where $B_z \approx 6$ kG, the beam is not stable and the power in the pump wave drops to zero—as suggested in figure 13. As a result, 10 kG was chosen as the basic operating point; it is not too high and the beam is stable and a healthy pump wave is produced. The presence of high-frequency stop-bands in the rippled wall slow-wave structure could also account for some of the amplitude variation with increasing harmonic number that is present in figures 21 and 22.

The wide range of frequencies accessible through this mechanism and its demonstrated tunability provide the basis for a wide range of applications. Some prospective uses would include spectroscopy, chemical reaction and process control, and laser isotope separation, in addition to the more "classical" applications such as remote sensing of the atmosphere, high-resolution radars, plasma heating, particle acceleration, and laser surgery. A more extensive discussion of FEL applications is given by Marshall [38].

This experiment represented a venture into unexplored areas of physics, and it was not always possible to be prepared for some of the results that were discovered. However, the experience gained in this series of experiments does provide some basis for structuring future studies.

In particular, the region between the slow-wave structure and the reflecting waveguide beyond cutoff should be extended to provide a longer interaction region that would give some of the instabilities more time to grow and possibly lead to higher output powers. Some sort of mode

selective device such as a Bragg cavity [57] could also be introduced to help maximize the power in some selected frequency range. It should also be possible to replace the waveguide cutoff region with a coupling cavity that would extract the pump wave rather than reflecting it back through the interaction region. This would eliminate the distraction of being always forced to look for forward wave interactions, and it could also lead to more efficient extraction of the power in the pump wave. The possibilities for operating the device as an amplifier should also be investigated.

In the diagnostic area, there are many opportunities for further study. The gap in the frequency measurements between the high and low ranges should be closed so that the gamut of peaks can be studied. A more comprehensive survey of the lower frequency range should be undertaken with axial horns replacing the radial coupling holes. As diagnostic sophistication grows, mode and radiation pattern information should be recorded, and of course the search should be renewed for the interaction frequencies on the up-shifted branch.

Finally it should be noted that (for the present) this is the only known area of FEL research in which there is more experimental than theoretical activity.

References

1. Y. Carmel, V. L. Granatstein, and A. Gover, Demonstration of a two-stage backward wave oscillator FEL, *Phys. Rev. Lett.* 51(7) (1983), 566.

2. G. G. Denisov et al., Powerful electromagnetic millimeter wave oscillations produced by stimulated scattering of microwave radiation by electron beams, *Int. J. Infrared and Millimeter Waves* 5(10) (1984), 1389.

3. G. Bekefi and R. E. Shefer, Stimulated Raman scattering by an intense relativistic electron beam subjected to a rippled electric field, *J. Appl. Phys.* 50(8) (1979), 5158.

4. B. Levush, T. M. Antonsen, Jr., W. Manheimer, and P. Sprangle, A free-electron laser with a rotating quadrupole wiggler, *Phys. Fluids* 28 (1985), 2273.

5. T. M. Antonsen, Jr., and B. Levush, Nonlinear theory of a quadrupole FEL, *IEEE J. Quantum Electron.* QE-23(9) (1987).

6. H. Motz, Applications of the radiation from fast electron beams, *J. Appl. Phys.* 22 (1951), 527.

7. H. Motz, W. Thon, and R. N. Whitehurst, Experiments on radiation by fast electron beams, *J. Appl. Phys.* 24 (1953), 826.

8. R. M. Phillips, The Ubitron, a high-power traveling wave tube based on a periodic beam interaction in unloaded waveguide, *IRE* ED-7 (1960), 231.

9. R. M. Phillips, The Ubitron as a high-power millimeter wave amplifier, *Proc. 4th Int. Congress on Microwave Tubes* (1962), 371.

10. C. E. Enderby and R. M. Phillips, The Ubitron amplifier—a high-power millimeter-wave TET, *IEEE Proc.* 53 (1965), 1648.

11. R. Jackson, D. E. Pershing, and F. Wood, NRL Ubitron amplifier cold test results, presented at Proc. 8th Int. FEL Conf., Glasgow, Scotland, published in *Nuc. Instrum. Methods* in *Phys. Res.* A259 (1987), 99.

12. R. H. Pantell, G. Soncini, and H. E. Puthoff, Stimulated photoelectron scattering, *IEEE J. Quantum Electron.* QE-4 (1968), 905.

13. J. M. J. Madey, Stimulated emission of bremsstrahlung in a periodic magnetic field, *J. Appl. Phys.* 42 (1971), 1906.

14. R. B. Palmer, Interaction of relativistic particles and free electromagnetic waves in the presence of a static helical magnetic, *J. Appl. Phys.* 43 (1972), 3014.

15. V. P. Sukhatme and P. E. Wolff, Stimulated Compton scattering as a radiation source—theoretical limitation, *J. Appl. Phys.* 44 (1973), 2331.

16. V. P. Sukhatme and P. E. Wolff, Stimulated magneto-Compton scattering—a possible tunable far-infrared and millimeter source, *IEEE J. Quantum Electron.* QE-10 (1974), 870.

17. L. R. Elias, W. M. Fairbank, J. M. J. Madey, H. A. Schwettman, and T. I. Smith, *Phys. Rev. Lett.* 36 (1976), 717.

18. D. A. G. Deacon, L. R. Elias, J. M. J. Madey, G. J. Ramian, H. A. Schwettman, and T. I. Smith, First operation of a free-electron laser, *Phys. Rev. Lett.* 38(16) (18 April 1977), 892.

19. V. L. Granatstein and P. Sprangle, Mechanisms for coherent scattering of electromagnetic waves from relativistic electron beams, *IEEE Trans.* MTT-25(6) (1977), 545.

20. V. L. Granatstein, S. P. Schlesinger, M. Herndon, R. K. Parker, and J. A. Pasour, Production of megawatt submillimeter pulses by stimulated magneto-Raman scattering, *Appl. Phys. Lett.* 30 (1977), 384.

21. D. B. McDermott, T. C. Marshall, S. P. Schlesinger, R. K. Parker, and V. L. Granatstein, High-power FEL based on stimulated Raman scattering, *Phys. Rev. Lett.* 41(20) (1978), 1368.

22. R. H. Jackson, S. H. Gold, R. K. Parker, H. P. Freund, P. C. Efthimion, V. L. Granatstein, M. Herndon, A. K. Kinkead, J. E. Kosakowski, and T. J. Kwan, Design and operation of a collective millimeter-wave free-electron laser, *IEEE J. Quantum Electron.* QE-19 (1983), 346.

23. S. H. Gold, W. M. Black, H. P. Freund, V. L. Granatstein, R. H. Jackson, P. C. Efthimion, and A. K. Kinkead, Study of gain, bandwidth, and tunability of a millimeter-wave FEL operating in the collective regime, *Phys. Fluids* 26 (1983), 2683.

24. T. J. Orzechowski, B. R. Anderson, J. C. Clark, W. M. Fawley, A. C. Paul, D. Prosnitz, E. T. Scharlemann, and S. M. Yarema, High-efficiency extraction of microwave radiation from a tapered wiggler free electon laser, *Phys. Rev. Lett.* 57(17) (27 October 1986), 2172.

25. J. Fajans, Radiation measurements of an intermediate energy FEL, Ph.D. thesis, MIT (1985).

26. H. P. Freund, S. Johnston, and P. Sprangle, Three-dimensional theory of FEL with an axial guide field, *IEEE J. Quant. Electron.* QE-19 (1983), 322.

27. P Sprangle, C. M. Tang, and W. M. Manheimer, Nonlinear theory of FEL and efficiency enhancement, *Phys. Rev.* A 21(1) (1980), 302.

28. H. P. Freund, Nonlinear analysis of FEL amplifiers with axial guide fields, *Phys. Rev.* A 27(4) (1983), 1977 .

29. A. S. El'chaninov, F. Ya. Zagulov, N. F. Kovalev, S. D. Korovin, N. V. Rostov, and A. V. Smorgonskii, Highly efficient relativistic backward wave tube, *Sov. Tech. Phys. Lett.* 6(4) (1980), 191.

30. Yu. F. Bondar et al., Measurements of RF emission from a carcinotron with a relativistic electron beam. *Sov. J. Plasma Phys.* 9(2) (1983), 223.

31. R. A. Kehs, A. Bromborsky, B. G. Ruth, S. E. Graybill, W. W. Destler, Y. Carmel, and M. C. Wang, A high-power backward wave oscillator driven by a relativistic electron beam, *IEEE Trans.* PS-13(6) (1985), 559.

32. V. L. Bratman, et al., Powerful millimeter-wave generators based on the stimulated Cerenkov radiation of relativistic electron beams, *Int. J. Infrared and Millimeter Waves* 5(9) (1984), 1311.

33. P. Sprangle, V. L. Granatstein, and L. Baker, Stimulated collective scattering from a magnetized relativistic electron beam, *Phys. Rev.* A 12(4) (1975), 1697.

34. H. P. Freund, R. A. Kehs, and V. L. Granatstein, Electron orbits in combined electromagnetic wiggler and axial guide magnetic fields, *IEEE J. Quantum Electron.* QE-21(7) (1985), 1080.

35. A. Goldring and L. Friedland, Electromagnetically pumped free electron laser with a guide magnetic field, *Phys. Rev.* A 32(5) (1985), 2879.

36. J. D. Jackson, *Classical Electrodynamics*, 2d ed., John Wiley and Sons (1975), 347.

37. R. E. Collin, *Foundations for Microwave Engineering*, McGraw-Hill, NY (1966).

38. T. C. Marshall, *Free Electron Lasers*, Macmillan Publishing Co., NY (1985).

39. C. C. Johnson, *Field and Wave Electrodynamics*, McGraw-Hill, NY (1965).

40. J. Fajans, G. Bekefi, Y. Z. Yin, and B. Lax, Microwave studies of a tunable FEL in combined axial and wiggler guide fields, *Phys. Fluids* 28(6) (1985), 1995.

41. P. C. Efthimion and S. P. Schlesinger, Stimulated Raman scattering by an intense relativistic electron beam in a long rippled magnetic field. *Phys. Rev.* A 16(2) (1977), 633.

42. A. A. Grossman and T. C. Marshall, A FEL oscillator based on a cyclotron undulator interaction, *IEEE J. Quantum Electron.* QE-19(3) (1983).

43. A. A. Grossman, T. C. Marshall, and S. P. Schlesinger, A new millimeter FEL using a relativistic electron beam with spiraling electrons, *Phys. Fluids* 26(1) (1983), 337.

44. R. A. Kehs, Y. Carmel, W. W. Destler, and V. L. Granatstein, Experimental demonstration of an electromagnetically-pumped FEL with cyclotron harmonic idlers, *Phys. Rev. Lett.* 60 (4) (25 January 1988).

45. J. L. Vomvorides, An efficient Doppler-shifted electron cyclotron maser oscillator, *Int. J. Elect.* 53(6) (1982), 555.

46. A. T. Lin, Doppler shift dominated cyclotron masers, *Int. J. Elect.* 57(6) (1984), 1097.

47. R. A. Kehs, G. A. Huttlin, A. Bromborsky, B. G. Ruth, S. E. Graybill, A. Shpilman, and M. J. Rhee, Dragon, a low impedance megavolt modulator for performing relativistic electron beam experiments, *Proc. 16th Power Modulator Symposium*, Rossalyn, VA (1984).

48. A. Bromborsky, private communication.

49. N. I. Zaitsev, N. F. Kovalev, B. D. Kol'chugin, and M. I. Fuks, Experimental investigation of a relativistic carcinotron, *Sov. Phys. Tech. Phys.* 27(8) (1982), 986.

50. V. S. Ivanov, S. I. Krementsov, V. A. Kutsenko, M. D. Raizer, A. A. Rukhadze, and A. V. Fedotov, Investigation of a relativistic Cerenkov self-generator, *Sov. Phys. Tech. Phys.* 26(5) (1981), 580.

51. S. A. Maas, *Microwave Mixers*, Artech House, Norwood, MA (1986).

52. B. G. Ruth, private communication.

53. J. Fisher, D. A. Boyd, A. Cavallo, and J. Benson, Ten-channel grating polychromator for electron cyclotron emission plasma diagnostics, *Rev. Sci. Instrum.* 54(9) (1983), 1085.

54. A. Shpilman, *Design Considerations, Implementation, and Testing of a Transformer Powered Pulse Generator*, MS thesis, University of MD (1983).

55. B. G. Ruth, *A Magnetic Field System for an Experimental BWO High-Power Microwave Source* (unpublished).

56. General catalog, Tektronix, Inc., Beaverton Oregon, 1987.

57. M. C. Wang, V. L. Granatstein, and R. A. Kehs, Design of a Bragg cavity for a millimeter-wave FEL, *Appl. Phys. Lett.* 48(13) (31 March 1986), 817.

Appendix A.—The Dragon REB Generator

This appendix describes the operation of the Dragon relativistic electron-beam generator that was used to provide the electron beam used in the experiments described in the main body of this report. The basic Dragon generator is shown schematically in figure A-1. After the primary capacitors, C_1, have been fully charged, switch S_1 is triggered and the energy stored in C_1 moves through the transformer to a transmission line represented by C_2. When the voltage on C_2 reaches its maximum, switch S_2 closes (self-breaks), and the energy on transmission line C_2 flows into the electron-beam diode, producing the intense relativistic electron beam used in the experiments. By properly tuning the LC circuits on the primary and secondary windings of the transformer, one can achieve the "dual resonance" operating mode in which all the energy stored in the primary capacitor bank will appear on the transmission line, C_2. A tuning inductor, L_t, is used to help ensure dual-resonance operation. The tuning inductor also helps to protect the transformer from potentially dangerous high-voltage spikes.

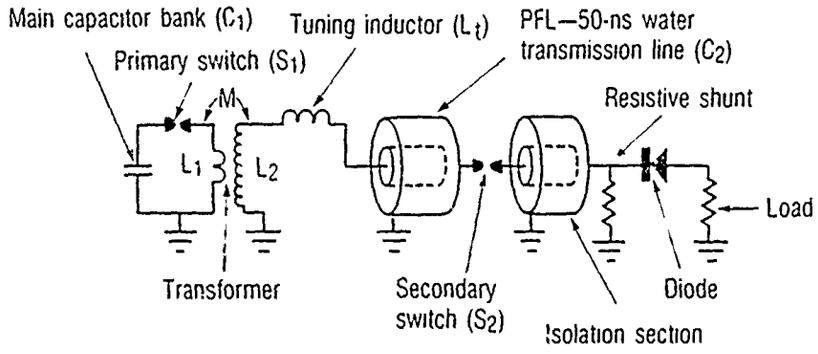

Figure A-1. Schematic drawing of Dragon relativistic electron-beam generator.

Figure A-2 shows a more graphic view of the Dragon system. The capacitor bank lives in an isolation box that can be filled with Freon for additional insulation. The capacitor bank is connected directly to the primary of the step-up transformer through the primary switch. The output of the transformer is coupled through the tuning inductor to a 6.5-Ω water-filled transmission line which is used as a pulse forming line (PFL). A self-breaking secondary switch connects the PFL to a section of time-isolation transmission line which feeds the diode. The diode consists of a variable-impedance dummy load, an axial insulator stack, and a standard anode-cathode gap electron-beam diode. The remainder of this appendix describes some of the major individual components in more detail.

The primary capacitor bank consists of eight 1.85-μF high-voltage capacitors. When charged to 50 kV, these capacitors store 18.5 kJ of energy. In the actual operating configuration, four capacitors are charged to +50 kV and four are charged to −50 kV. Their connection to the primary of the transformer is shown in figure A-3.

A split single-turn primary (isolated from the secondary) was used in place of the more conventional autotransformer. This allowed the minimization of insulation, volume, and power supply requirements. Also in this configuration, the highest voltage with respect to ground (outside the transformer) is 50 kV, which can be easily insulated with Mylar and Freon gas. The capacitor cases remain at ground during discharge.

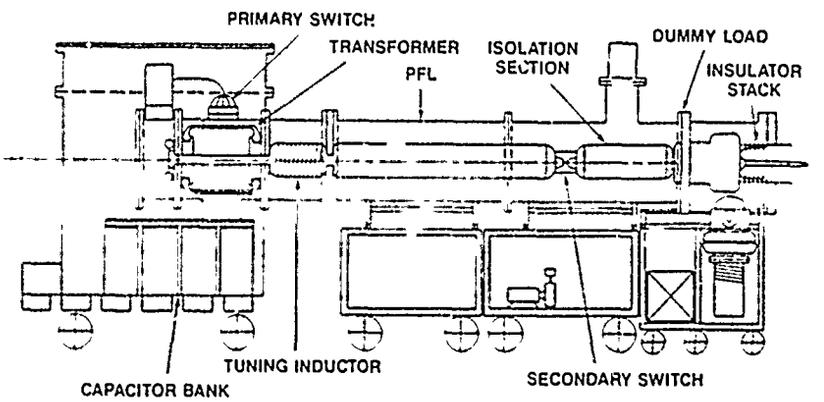

Figure A-2. Graphical representation of Dragon relativistic electron-beam generator.

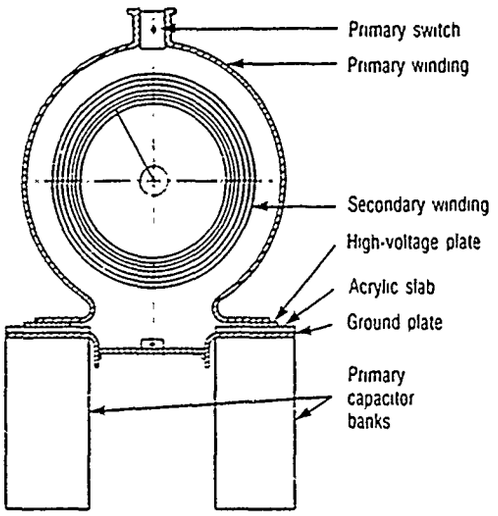

Figure A-3. Idealized drawing of Dragon voltage step-up transformer.

The voltage step-up transformer is designed to work in the dual resonance mode [1,2]. When this condition is satisfied, all of the energy stored in the primary capacitor bank will periodically appear on the PFL. The conditions for dual resonance are achieved by (1) setting

$$k = \frac{M}{\sqrt{L_1(L_2 + L_t)}} = 0.6, \qquad (A-1)$$

where k is the coupling constant and M is the mutual inductance, and (2) setting

$$L_1C_1 = L_2C_2. \qquad (A-2)$$

The secondary on the Dragon transformer currently contains 31 turns.

The PFL represented by C_2 in figure A-1 is a water-filled transmission line with an electrical length of 50 ns. The outer and inner diameters are 23.5 and 9 in., which results in a characteristic impedance of 6.5 Ω. The 23-ns isolation section separates (by 46 ns) the main pulse initiated by the secondary switch closure from any postpulse due to reflection at a mismatched load. The isolation section also serves as a capacitive divider to suppress any prepulse on the diode.

The pulse forming line is terminated with a dummy load shunted by the anode-cathode diode. This disk-shaped load provides an approximately matched termination to the 6.5-Ω PFL. With this dummy load

the high-impedance diode has a miniscule effect on the voltage driving the diode. Because of the relatively large size of the geometry, aluminum electrodes were used with sodium thiosulfate as the electrolyte. The solution is continuously circulated to the outside world, where its concentration can be easily adjusted as necessary.

The operation of the Dragon machine is described in more detail by Kehs [3] and Shpilman [2].

References

1. G. J. Rohwein, A three megavolt transformer for PFL charging, *IEEE Trans.* NS-26 (1979), 4211.

2. A. Shpilman, *Design considerations, implementation, and testing of a transformer powered pulse generator*, MS thesis, University of MD (1983).

3. R. A. Kehs, G. A. Huttlin, A. Bromborsky, B. G. Ruth, S. E. Graybill, A. Shpilman, and M. J. Rhee, DRAGON, a low impedance megavolt modulator for performing relativistic electron beam experiments, *Proc. 16th Power Modulator Symposium*, Rossalyn, VA (1984).

Appendix B.—The BWO Pump Wave

B-1 Introduction

The backward wave oscillator (BWO) used in these experiments is a physically simple device in which an intense relativistic electron beam (IREB) is passed through a rippled wall type of slow-wave structure as shown in figure B-1. The beam interacts with the slow-wave structure in such a way that some of the beam's kinetic energy is coupled into the propagating electromagnetic modes of the slow-wave structure. This is accomplished through the growth of negative-energy space charge waves on the IREB. The mode, frequency, and intensity of the generated microwave radiation are determined by the geometry of the slow-wave structure and the electron beam.

Since the electron beam is discussed in section 3.2 (in the main body of text), the following sections present the slow-wave structure and describe how it was used to couple the beam's kinetic energy into the propagating TM_{01} mode in the structure.

B-2 The Physical Picture

The slow-wave structure used in these experiments is the rippled wall waveguide shown in figure B-1. This type of structure was chosen because it is less susceptible to the high field breakdown problems found in such conventional devices as the helix- and iris-loaded waveguides. Physically, the actual device was constructed by plating a thin layer of copper onto an aluminum mandrel that was machined to the desired inner dimensions of the slow-wave structure on a numerically controlled lathe. The copper-plated aluminum piece was then cast in an epoxy support structure and the aluminum was etched away with a sodium hydroxide solution, leaving the finished slow-wave structure. The physical dimensions of the structure were chosen to match those of Bondar

et al. [1] so that analysis techniques [2] could be checked with results reported by Bondar et al. [1].

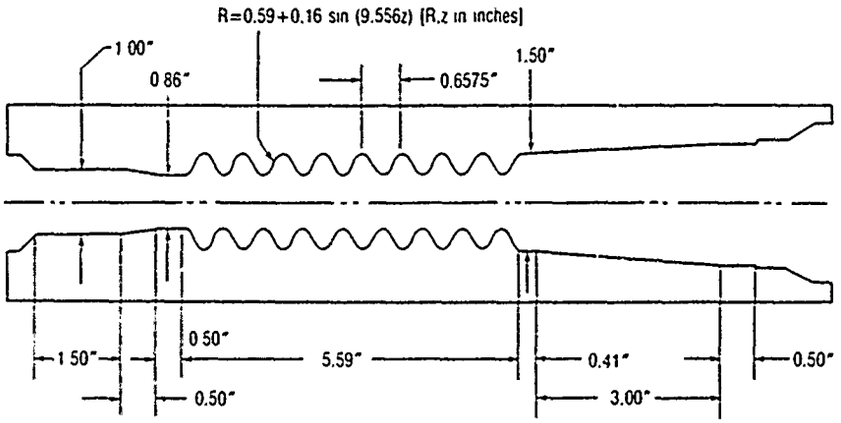

Figure B-1. Rippled wall slow-wave structure.

B-3 The Empty-Waveguide Dispersion Relation

In order to analyze the effect of the slow-wave structure on the electron beam, one must first determine which modes and frequencies are able to propagate in the structure. Since the electron beam is primarily directed in the $\hat{z}$ direction and is axially symmetric, one anticipates coupling of beam energy to the TM_{0n} modes of the structure. The Maxwell equations can be solved for an infinitely long structure with the ripple given in figure B-1. The results are summarized in the dispersion relation shown in figure B-2. Note the small extent of the pass bands, which indicates that $|d\omega/dk_z| \ll c$ everywhere within the pass band, implying large E_z fields and good coupling to space charge waves. The next step is to plot the space charge wave dispersion relation

$$\omega = v_{\parallel}(k - 2\pi n/L), \qquad (B-1)$$

(where $v_{\parallel}$ is the beam axial velocity, n is the spatial harmonic, and L is the ripple period in the slow-wave structure) on the same axes as the empty structure dispersion relation.

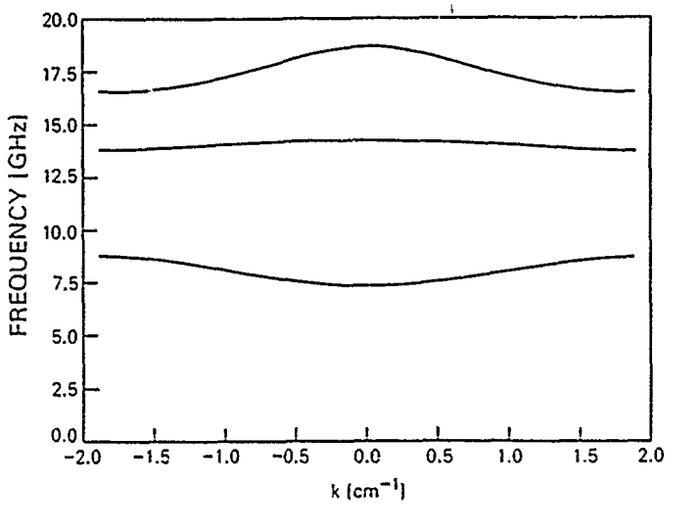

Figure B-2. Empty-waveguide dispersion diagram for low-order TM_{0n} modes.

B-4 Beam Dispersion Relation

The addition of the space charge waves to the empty waveguide dispersion relation results in the plot shown in figure B-3. The space charge waves which propagate at the beam velocity are the source of the energy that couples into the structure's propagating electromagnetic modes and drives the BWO interaction. The operating frequency of the BWO is well approximated by the intersection of the $n = -1$ spatial harmonic of the space charge wave with the $n = 0$ spatial harmonic ($-\pi \leq k_z L \leq \pi$) of the empty waveguide mode (i.e., the TM_{01} mode). Note that this point is equivalent to the operating point determined by the intersection of the $n = 0$ spatial harmonic ($\pi \leq k_z L \leq 3\pi$) of the empty waveguide mode in the sense that the frequency, fields, and beam quantities associated with each operating point are identical. However, the phase velocity of the BWO wave is different at each operating point.

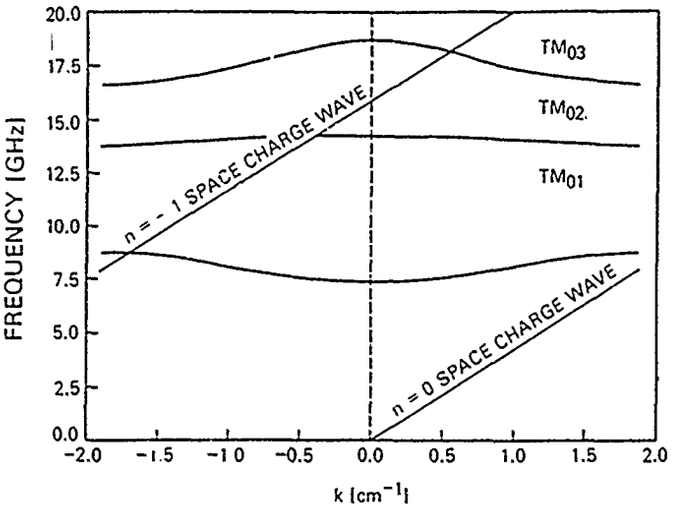

Figure B-3. Empty-waveguide dispersion diagram with superimposed ideal beam waves added.

Also note that two axially propagating space charge waves are supported by the electron beam [3]: fast ($v_{ph} > v_{\|}$) and slow ($v_{ph} < v_{\|}$) space charge waves. The actual dispersion relation is approximated by

$$\omega = v_{\|}(k - 2\pi n/L) \pm \omega_b, \qquad (B-2)$$

where ω_b is the beam electron plasma frequency. Thus, the plot in figure B-3 is valid only when ω_b is small.

The intersection point of the space charge wave line with the periodic electromagnetic wave dispersion relation is the operating point of the device. The full beam dispersion relation easily yields the possible frequencies and modes of operation. Note that the intersection point in figure B-3 lies on a portion of the electromagnetic wave dispersion relation where $d\omega/dk < 0$, which implies a backward propagating wave.

The above discussion of dispersion relations is highly idealized. In actual practice, coupling between the space charge and electromagnetic waves results in a far more complicated region of intersection [4,5] in which the actual operating point will be complex—with the imaginary portion representing the growth rate of the instability. An "in depth" discussion is beyond the scope of this report, although more detailed expositions are found elsewhere [4-6].

References

1. Yu. F. Bondar et al., Measurements of RF emission from a carcinotron with a relativistic electron beam, *Sov. J. Plasma Phys.* 9(2) (1983), 223.

2. A. Bromborsky and B. G. Ruth, Calculation of the TM_{0n} dispersion relations in a corrugated cylindrical waveguide, *IEEE Trans.* MTT-32(6) (1984).

3. C. C. Johnson, *Field and Wave Electrodynamics*, McGraw-Hill, NY (1965).

4. J. A. Swegle, J. W. Poukey, and G. T. Leifeste, Backward wave oscillators with rippled wall resonators: Analytic theory and numerical simulation, *Phys. Fluids* 28(9) (1985), 2882.

5. R. J. Briggs, *Electron Stream Interaction with Plasmas*, MIT Press, Cambridge, MA (1964).

6. J. A. Swegle, Approximate treatment near resonance of backward and traveling wave tubes in the Compton regime, *Phys. Fluids* 28(12) (1985), 3696.

Appendix C.—The Microwave Grating Spectrometer

The spectrometer used in these experiments was the prototype of a system that was designed by the University of Maryland's Lab for Plasma Fusion Energy Studies for measuring the electron cyclotron emission from tokamak plasmas [1]. It is similar to the microwave spectrometers used by other researchers in the high-power, high-frequency reigme [2-4]. The operational frequency range was extended from the original design of 90 to 140 GHz to 50 to 200 GHz by the construction of additional gratings. A detailed description of scattering from a diffraction grating [5-7] is beyond the scope of this report; however, the elementary theory and operation are developed and discussed in this appendix.

A schematic drawing of the spectrometer configuration is shown in figure C-1. The microwave radiation enters via the input horn and illuminates the mirror M1 which deflects the radiation through a lens and onto the grating. The scattered radiation from the grating then reflects off mirror M2 and into the pickup horn which feeds the microwave detector.

The effective scattering by the grating is given by the condition for constructive interference. If each grating line is considered a point source, then by equating the wave path lengths as shown in figure C-2, the familiar form for the constructive interference condition may be easily expressed as

$$d(\sin\theta_i - \sin\theta_r) = \lambda, \qquad (C-1)$$

where d is the spacing between adjacent gratings and λ is the wavelength of the wave under consideration. The local convention has been to describe the configuration in a state in which both the incident and reflected rays are on the same side of the normal to the grating. Thus, the condition for constructive interference becomes

$$d(\sin\theta_i + \sin\theta_r) = \lambda. \qquad (C-2)$$

With this convention, the useful range of grating angles, θ_i (for reasonably flat frequency response), is approximately $-2°$ to $+8°$.

Note that in figure C-1, the angle $\theta_r - \theta_i = \alpha = \text{constant}$. One may eliminate θ_r in favor of α to obtain

$$\sin\theta_i + \sin(\alpha + \theta_i) = \lambda/d. \qquad (C-3)$$

The substitution $\lambda = c/f$ and judicious use of half-angle formulas may be combined with equation (C-3) to reach

$$\theta_i = -\frac{\alpha}{2} + \arcsin\left[\frac{c/fd}{2\cos(\alpha/2)}\right], \qquad (C-4)$$

which gives the grating angle θ_i needed to detect a given input frequency, f. This formula was used to build the tables of θ_i for various values of f and d that were used to set the spectrometer for the desired frequency measurements.

The initial setup of the spectrometer was facilitated by the use of a small He-Ne laser that was mounted in place of the microwave input horn. The relative zero angle on the angular scale (attached to the grating) was determined by the position at which a mirror on the surface of the grating reflected the laser beam straight back along its original path. Actually, the laser was slightly tilted so that the reflected beam did not reenter the source. The grating (with mirror) was then rotated until the laser beam struck the center of the receiving horn, providing a measure of the angle $\alpha/2$ in figure C-1. In actual practice, the mirror is attached to the nongrating side of the grating plate, and the zero angle must be "corrected" by 180°.

Further calibration was achieved by launching a known microwave signal into the spectrometer and viewing the detector output as a function of grating angle. The results indicated that equation (C-4) is a highly accurate predictor of spectrometer operation. The FWHM of the detector signal divided by the base frequency gave $\Delta f/f \sim 0.02$, which is close to the resolving power quoted by Fisher [1]. The linewidth of the input "calibration" signal was not known.

The grating spectrometer was a reliable "work horse" that provided no surprises and always functioned as predicted by the simple models described above.

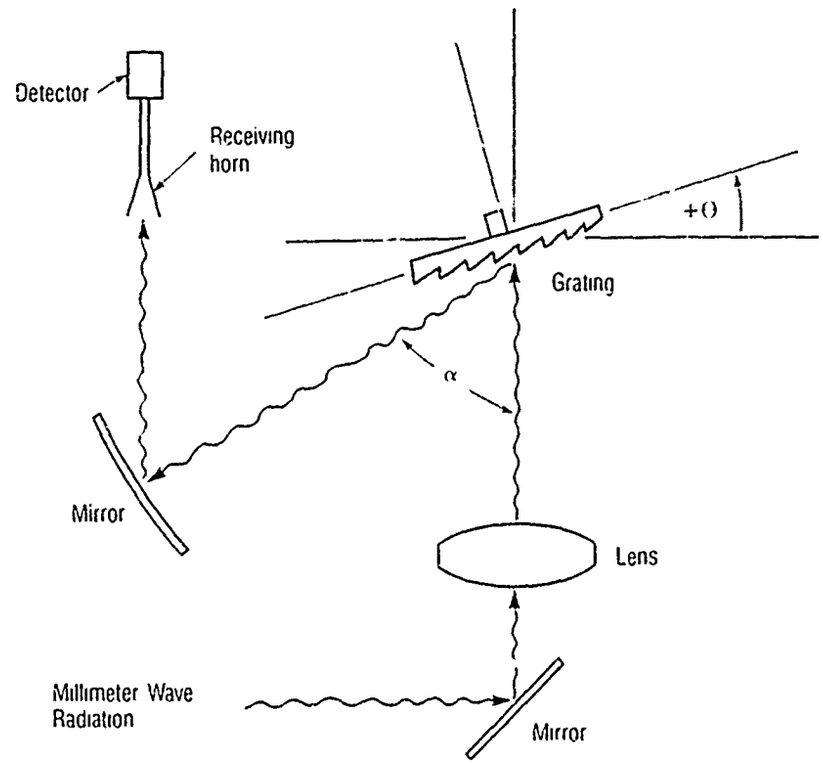

Figure C-1. Schematic drawing of grating spectrometer.

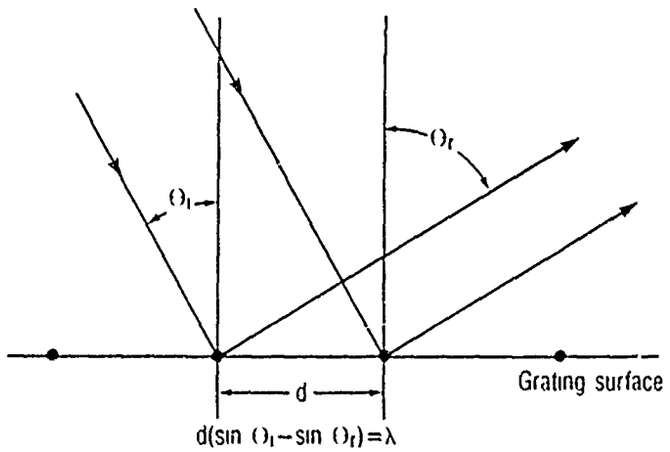

Figure C-2. Simple model of condition for constructive interference from a diffraction grating.

References

1. J. Fisher, D. A. Boyd, A. Cavallo, and J. Benson, Ten-channel grating polychromator for electron cyclotron emission plasma diagnostics, *Rev. Sci. Instrum.* 54(9) (1983), 1083.

2. W. M. Bollen, R. H. Jackson, D. J. Sullivan, and D. E. Voss, A grating spectrometer for millimeter waves, *Proc. IEEE Int. Conf. on Plasma Sci.*, San Diego, CA (1983).

3. J. A. Pasour and S. P. Schlesinger, Multichannel grating spectrometer for millimeter waves, *Rev. Sci. Instrum.* 48(10) (1977), 1355.

4. R. M. Gilgenbach, T. C. Marshall, and S. P. Schlesinger, Spectral properties of stimulated Raman radiation from an intense relativistic electron beam, *Phys. Fluids* 22(5) (1979), 971.

5. D. Maystre, Rigorous vector theories of diffraction gratings, in *Progress in Optics*, vol 21, ed by E. Wolf, North-Holland Physics Pub, Amsterdam (1984).

6. E. G. Loewen, M. Neviere, and D. Maystre, Grating efficiency theory as it applies to blazed and holographic gratings, *Appl. Opt.* 16(10) (1977), 2711.

7. M. Born and E. Wolf, *Principles of Optics*, 6th ed, Pergamon Press (1980).

DISTRIBUTION

DIRECTOR
DEFENSE TECHNICAL INFORMATION
CENTER
ATTN DTIC-DDA (2 COPIES)
CAMERON STATION, BUILDING 5
ALEXANDRIA, VA 22304-6145

AIR FORCE WEAPONS LAB
ATTN DR. W. BAKER
ATTN DR. B. B. GODFREY
ATTN DR. K. HACKETT
KIRTLAND AFB
ALBUQUERQUE, NM 87117

COLUMBIA UNIVERSITY
DEPARTMENT OF ELECTRICAL
ENGINEERING
ATTN DR. S. SCHLESINGER
520 WEST 120TH STREET
NEW YORK, NY 10027

COLUMBIA UNIVERSITY
DEPARTMENT OF APPLIED PHYSICS
& NUCLEAR ENGINEERING
ATTN T. C. MARSHALL
ATTN R. GROSS
520 WEST 120TH STREET
NEW YORK, NY 10027

CORNELL UNIVERSITY
SCHOOL OF APPLIED & ENGINEERING
PHYSICS
ATTN PROF. H. H. FLEISCHMANN
ATTN PROF. J. NATION
ATTN PROF. R. N. SUDAN
ATTN PROF. C. B. WHARTON
ITHICA, NY 14853

DARTMOUTH COLLEGE
ATTN DR. J. E. WALSH
18 WILDER, BOX 6127
HANOVER, NH 03755

LAWRENCE LIVERMORE NATIONAL
LABORATORY
ATTN DR. J. CHASE
ATTN DR. T. J. ORZECHOWSKI
ATTN F. CAMACHO
ATTN DR. J. SWEGLE
PO BOX 808
LIVERMORE, CA 94550

LOS ALAMOS SCIENTIFIC LABORATORY
ATTN DR. R. R. BARTSCH
ATTN DR. C. BRAU
ATTN DR. H. A. DAVIS
ATTN DR. W. HOEBERLING
ATTN DR. T.J.T. KWAN
ATTN DR. P. J. O'SHEA

LOS ALAMOS SCIENTIFIC LABORATORY
(cont'd)
ATTN DR. L. THODE
PO BOX 1663, AT5-817
LOS ALAMOS, NM 87545

MASSACHUSETTS INSTITUTE OF
TECHNOLOGY
DEPARTMENT OF PHYSICS
ATTN DR. G. BEKEFI/36-213
ATTN DR. R. DAVIDSON/NW 16-206
ATTN DR. A. BERS/NW 38-260
DR. K. KREISCHER
CAMBRIDGE, MA 02139

MASSACHUSETTS INSTITUTE OF
TECHNOLOGY
ATTN DR. B. DANLEY/NW 16-174
ATTN DR. R. TEMKIN/NW 14-4107
167 ALBANY ST., NW 16-200
CAMBRIDGE, MA 02139

MISSION RESEARCH CORPORATION
SUITE 201
ATTN DR. M. BOLLEN
ATTN DR. T. HARGREAVES
ATTN DR. J. McADOO
ATTN DR. J. PASOUR
ATTN L. SMUTEK
5503 CHEROKEE AVE
ALEXANDRIA, VA 22312

MISSION RESEARCH CORPORATION
ATTN D. SULLIVAN
1720 RANDOLPH ROAD, SE
ALBUQUERQUE, NM 87106

NAVAL RESEARCH LABORATORY
ATTN CODE 4000, W. ELLIS
ATTN CODE 4600, D. NAGEL
ATTN CODE 4710, C. KAPETANAKOS
ATTN CODE 4740, A. FLIFLET
ATTN CODE 4740, S. GOLD
ATTN CODE 4740, A. KINKEAD
ATTN CODE 4740, W. M. MANHEIMER
ATTN CODE 4770, G. COOPERSTEIN
ATTN CODE 4790, Y. Y. LAU
ATTN CODE 4790, P. SPRANGLE
ATTN CODE 4790, DR. C. M. TANG
ATTN CODE 6840, S. Y. AHN
ATTN CODE 6840, A. GANGULY
ATTN CODE 6840, DR. R. JACKSON
ATTN CODE 6804, R. K. PARKER
4555 OVERLOOK AVE SW
WASHINGTON, DC 20375

DISTRIBUTION (cont'd)

OFFICE OF NAVAL RESEARCH
ATTN DR. C. ROBERSON
300 N QUINCY STREET
ARLINGTON, VA 22217

NAVAL SURFACE WEAPONS CENTER
ATTN DR. H. S. UHM
ATTN DR. R. SCHNEIDER
ATTN V. KENYON
WHITE OAK LAB
SILVER APRING, MD 20903-5000

MAXWELL LABS, INC
ATTN DR. A. KOLB
8835 BALBOA AVE
SAN DIEGO, CA 92123

PHYSICS INTERNATIONAL
ATTN DR. J. BENFORD
ATTN DR. H. SZE
2700 MERCED STREET
SAN LEANDRO, CA 94577

PHYSICAL SCIENCE INC
ATTN M. READ
603 KING STREET
ALEXANDRIA, VA 22314

QUANTUM INSTITUTE
UNIVERSITY OF CALIFORNIA
ATTN DR. L. ELIAS
SANTA BARBARA, CA 93106

SANDIA NATIONAL LABORATORIES
ATTN J. E. POWELL
ATTN DR. J. HOFFMAN
ATTN DR. W. P. BALLARD
ATTN C. CLARK
ATTN K. PRESTWICH
ORG. 1231, PO BOX 5800
ALBUQUERQUE, NM 87185

SCIENCE APPLICATIONS, INC
ATTN DR. A. DROBOT
ATTN DR. H. FREUND
ATTN DR. A. WAI
1710 GOODRIDGE DR
McLEAN, VA 22102

UNIVERSITY OF CALIFORNIA
PHYSICS DEPARTMENT
ATTN DR. G. BENFORD
ATTN DR. N. ROSTOKER
IRVINE, CA 92717

UNIVERSITY OF CALIFORNIA
DEPARTMENT OF PHYSICS
ATTN DR. A. T. LIN
ATTN DR. N. LUHMANN

UNIVERSITY OF CALIFORNIA
(cont'd)
ATTN D. McDERMOTT
LOS ANGELES, CA 90024

UNIVERSITY OF MARYLAND
DEPARTMENT OF ELECTRICAL
ENGINEERING
ATTN DR. V. L. GRANATSTEIN
(5 COPIES)
ATTN DR. W. W. DESTLER (5 COPIES)
COLLEGE PARK, MD 20742

UNIVERSITY OF MARYLAND
LABORATORY FOR PLASMA & FUSION
ENERGY STUDIES
ATTN D. ABE
ATTN WEI-RAN JOIS
ATTN DR. Y. CARMEL (10 COPIES)
ATTN DR. B. LEVUSH
ATTN DR. T. ANTONSEN
ATTN DR. E. OTT
COLLEGE PARK, MD 20742

UNIVERSITY OF TENNESSEE
DEPT OF ELECTRICAL ENGR
ATTN DR. I. ALEXEFF
KNOXVILLE, TN 37916

UNIVERSITY OF UTAH
DEPARTMENT OF ELECTRICAL
ENGINEERING
ATTN DR. L. BARNETT
ATTN DR. J. M. BAIRD
3053 MERRILL ENGINEERING BLDG
SALT LAKE CITY, UT 84112

US NAVAL ACADEMY
ANNAPOLIS, MD 21402-5021

VARIAN ASSOCIATED
ATTN DR. H. JORY
ATTN DR. D. STONE
ATTN DR. K. FELCH
ATTN DR. A. SALOP
611 HANSEN WAY
PALO ALTO, CA 94303

VARIAN ASSOCIATES
ATTN DR. R. SMITH
ATTN G. THOMAS
ATTN DR. T. TREADO
8 SALEM RD
BEVERLY, MA 01915

US ARMY LABORATORY COMMAND
ATTN TECHNICAL DIRECTOR, AMSLC-TD

DISTRIBUTION (cont'd)

INSTALLATION SUPPORT ACTIVITY
ATTN LEGAL OFFICE, SLCIS-CC

USAISC
ATTN TECHNICAL REPORTS BRANCH,
AMSLC-IM-TR (2 COPIES)

HARRY DIAMOND LABORATORIES
ATTN D/DIVISION DIRECTORS
ATTN LIBRARY, SLCHD-TL (3 COPIES)
ATTN LIBRARY, SLCHD-TL (WOODBRIDGE)
ATTN CHIEF, SLCHD-NW-CS
ATTN CHIEF, SLCHD-NW-E
ATTN CHIEF, SLCHD-NW-EH
ATTN CHIEF, SLCHD-NW-EP
ATTN CHIEF, SLCHD-NW-ES
ATTN CHIEF, SLCHD-NW-P
ATTN CHIEF, SLCHD-NW-R
ATTN CHIEF, SLCHD-NW-RP
ATTN CHIEF, SLCHD-NW-RS
ATTN CHIEF, SLCHD-NW-TN
ATTN CHIEF, SLCHD-NW-TS
ATTN N. BERG, AMCLD-S3
ATTN J. SILVERSTEIN, AMCLD-S3
ATTN A. SINDORIS, AMCLD-S3
ATTN J. SATTLER, SLCHD-CS
ATTN D. BASSET, SLCHD-HPM
ATTN E. BROWN, SLCHD-HPM
ATTN S. GRAYBILL, SLCHD-HPM
ATTN J. INGRAM, SLCHD-NW-E
ATTN R. CHASE, SLCHD-NW-EP
ATTN W. SCOTT, SLCHD-NW-ES
ATTN C. FAZI, SLCHD-NW-CS
ATTN R. KAUL, SLCHD-NW-CS
ATTN J. KRECK, SLCHD-NW-CS

HARRY DIAMOND LABORATORIES
(cont'd)
ATTN L. JASPER, SLCHD-NW-CS
ATTN J. TATUM, SLCHD-NW-CS
ATTN M. ABE, SLCHD-NW-P
ATTN J. CORRIGAN, SLCHD-NW-P
ATTN J. GWALTNEY, SLCHD-NW-P
ATTN T. OLDHAM, SLCHD-NW-RP
ATTN F. J. AGEE, SLCHD-NW-RS
ATTN H. E. BRANDT, SLCHD-NW-RS
ATTN H. BRISKER, SLCHD-NW-RS
ATTN A. BROMBORSKY, SLCHD-NW-RS
ATTN D. DAVIS, SLCHD-NW-RS
ATTN G. HUTTLIN, SLCHD-NW-RS
ATTN L. F. LIBELO, SLCHD-NW-RS
ATTN M. LITZ, SLCHD-NW-RS
ATTN K. KERRIS, SLCHD-NW-RS
ATTN B. RUTH, SLCHD-NW-RS
ATTN J. SOLN, SLCHD-NW-RS
ATTN D. WHITTAKER, SLCHD-NW-RS
ATTN H. EISEN, SLCHD-NW-TS
ATTN J. DAVIS, SLCHD-R
ATTN P. JOHNSON, SLCHD-ST
ATTN W. WEIBACH, SLCHD-ST-MW
ATTN D. COOK, SLCHD-ST-AR
ATTN R. LEAVITT, SLCHD-ST-AP
ATTN C. MORRISON, SLCHD-ST-AP
ATTN M. TOBIN, SLCHD-ST-AP
ATTN D. WORTMAN, SLCHD-ST-AP
ATTN H. DROPKIN, SLCHD-ST-SP
ATTN J. NEMARICH, SLCHD-ST-SP
ATTN Z. SZTANKAY, SLCHD-ST-SP
ATTN P. INGERSOLL, SLCHD-TA
ATTN P. EMMERMAN, SLCHD-TA-AS
ATTN R. A. KEHS, SLCHD-NW-RS (25 COPIES)